

Dark Energy Survey Year 1 Results: Methods for Cluster Cosmology and Application to the SDSS

M. Costanzi,¹ E. Rozo,² M. Simet,³ Y. Zhang,⁴ A. E. Evrard,^{5,6} A. Mantz,⁷ E. S. Rykoff,^{7,8} T. Jeltema,⁹ D. Gruen,^{7,8} S. Allen,¹⁰ T. McClintock,² A. K. Romer,¹¹ A. von der Linden,¹² A. Farahi,¹³ J. DeRose,^{10,7} T. N. Varga,^{14,1} J. Weller,^{15,14,1} P. Giles,¹¹ D. L. Hollowood,⁹ S. Bhargava,¹⁶ A. Bermeo-Hernandez,¹⁶ X. Chen,⁶ T. M. C. Abbott,¹⁷ F. B. Abdalla,^{18,19} S. Avila,²⁰ K. Bechtol,²¹ D. Brooks,¹⁸ E. Buckley-Geer,⁴ D. L. Burke,^{7,8} A. Carnero Rosell,^{22,23} M. Carrasco Kind,^{24,25} J. Carretero,²⁶ M. Crocce,^{27,28} C. E. Cunha,⁷ L. N. da Costa,^{22,23} C. Davis,⁷ J. De Vicente,²⁹ H. T. Diehl,⁴ J. P. Dietrich,^{15,30} P. Doel,¹⁸ T. F. Eifler,^{31,32} J. Estrada,⁴ B. Flaugher,⁴ P. Fosalba,^{27,28} J. Frieman,^{4,33} J. García-Bellido,³⁴ E. Gaztanaga,^{27,28} D. W. Gerdes,^{5,6} T. Giannantonio,^{35,36,1} R. A. Gruendl,^{24,25} J. Gschwend,^{22,23} G. Gutierrez,⁴ W. G. Hartley,^{18,37} K. Honscheid,^{38,39} B. Hoyle,^{14,1} D. J. James,⁴⁰ E. Krause,³¹ K. Kuehn,⁴¹ N. Kuropatkin,⁴ M. Lima,^{42,22} H. Lin,⁴ M. A. G. Maia,^{22,23} M. March,⁴³ J. L. Marshall,⁴⁴ P. Martini,^{38,45} F. Menanteau,^{24,25} C. J. Miller,^{5,6} R. Miquel,^{46,26} J. J. Mohr,^{15,30,14} R. L. C. Ogando,^{22,23} A. A. Plazas,³² A. Roodman,^{7,8} E. Sanchez,²⁹ V. Scarpine,⁴ R. Schindler,⁸ M. Schubnell,⁶ S. Serrano,^{27,28} I. Sevilla-Noarbe,²⁹ E. Sheldon,⁴⁷ M. Smith,⁴⁸ M. Soares-Santos,⁴⁹ F. Sobreira,^{50,22} E. Suchyta,⁵¹ M. E. C. Swanson,²⁵ G. Tarle,⁶ D. Thomas,²⁰ and R. H. Wechsler^{10,7,8}

(DES Collaboration)

24 October 2018

ABSTRACT

We perform the first blind analysis of cluster abundance data. Specifically, we derive cosmological constraints from the abundance and weak-lensing signal of redMaPPer clusters of richness $\lambda \geq 20$ in the redshift range $z \in [0.1, 0.3]$ as measured in the Sloan Digital Sky Survey (SDSS). We simultaneously fit for cosmological parameters and the richness–mass relation of the clusters. For a flat Λ CDM cosmological model with massive neutrinos, we find $S_8 \equiv \sigma_8(\Omega_m/0.3)^{0.5} = 0.79^{+0.05}_{-0.04}$. This value is both consistent and competitive with that derived from cluster catalogues selected in different wavelengths. Our result is also consistent with the combined probes analyses by the Dark Energy Survey (DES) and the Kilo-Degree Survey (KiDS), and with the Cosmic Microwave Background (CMB) anisotropies as measured by *Planck*. We demonstrate that the cosmological posteriors are robust against variation of the richness–mass relation model and to systematics associated with the calibration of the selection function. In combination with Baryon Acoustic Oscillation (BAO) data and Big-Bang Nucleosynthesis (BBN) data (Cooke et al. 2016), we constrain the Hubble rate to be $h = 0.66 \pm 0.02$, independent of the CMB. Future work aimed at improving our understanding of the scatter of the richness–mass relation has the potential to significantly improve the precision of our cosmological posteriors. The methods described in this work were developed for use in the forthcoming analysis of cluster abundances in the DES. Our SDSS analysis constitutes the first part of a staged-unblinding analysis of the full DES data set.

Key words: cosmology: cluster, cluster: general

1 INTRODUCTION

Galaxy clusters form from the high density peaks of the initial matter distribution. As such, they bear the imprints of the statistical properties of the matter density field and its growth (for reviews, see e.g. Allen et al. 2011; Kravtsov & Borgani 2012). The abun-

dance of galaxy clusters has been used since the late 90’s to constrain the mean matter density of the Universe, Ω_m , and the amplitude of the density fluctuations in terms of σ_8 , the present-day rms of the linear density field in spheres of $8h^{-1}$ Mpc radii (e.g. Eke et al. 1998; Henry 2000; Borgani et al. 2001; Pierpaoli et al. 2001;

2 DES Collaboration

Reiprich & Böhringer 2002; Henry 2004, for early works). Constraints on σ_8 are especially powerful in combination with measurements of the amplitude of the matter power spectrum at high redshift — e.g. from CMB data — enabling us to study the growth of density perturbations over cosmic time. These studies allow us to place constraints on parameters such as the total neutrino mass, the dark energy equation of state, and parameters governing modified gravity models.

Current studies using cluster catalogs selected in the X-ray, optical, and millimeter wavelengths, provide consistent constraints on σ_8 and Ω_m (e.g. Vikhlinin et al. 2009; Rozo et al. 2010; Mantz et al. 2010, 2015; Planck Collaboration et al. 2016b; de Haan et al. 2016). These data have been also used in combination with H_0 and Baryon Acoustic Oscillation (BAO) priors to place competitive constraints on the dark energy equation of state parameter, modification of gravity and neutrino masses (e.g. Burenin & Vikhlinin 2012; Mantz et al. 2010, 2015; Cataneo et al. 2015; Planck Collaboration et al. 2016b; de Haan et al. 2016). Ongoing — e.g. the Dark Energy Survey (DES)¹, the Hyper Suprime-Cam² — and forthcoming — the Large Synoptic Survey Telescope³, Euclid⁴, eROSITA⁵ — wide-area surveys aim to use clusters samples with an order of magnitude more systems than previous analyses in order to improve upon current constraints.

The most critical difficulty that cluster abundance studies must confront is the fact that cluster masses are not easily measured, forcing us to rely on observational proxies that correlate with mass. Specifically, while it is possible to predict the abundance of dark matter halos as a function of mass in an arbitrary cosmology with percent level accuracy (e.g. Sheth & Tormen 1999; Tinker et al. 2008; Crocce et al. 2010; Bocquet et al. 2016; McClintock et al. 2018a), halo masses themselves are not directly observable. At present, cosmological constraints from cluster abundance analyses at all wavelengths are limited by the uncertainty in the calibration of the relation between the cluster mass and the observable property used as a mass proxy, be it richness (i.e. count of member galaxies), X-ray luminosity, or the thermal Sunyaev-Zeldovich signal.

Currently, weak gravitational lensing measurements provide the gold-standard technique for estimating cluster masses (see e.g. von der Linden et al. 2014b, for a discussion). The weak lensing signal, i.e. the tangential alignment of background galaxies around the foreground cluster due to gravitational lensing, is a well-understood effect, sensitive to both dark and baryonic matter. Moreover, in contrast to other techniques (e.g. velocity dispersion and hydrostatic mass measurements), weak lensing mass measurements do not rely on assumptions about the dynamical state of the cluster. Despite these advantages, many sources of systematic error do affect this type of measurement, e.g. shear and photometric redshift biases, halo triaxiality, and projection effects. These systematics represent a significant amount of the total error budget of many recent studies (e.g. von der Linden et al. 2014a; Hoekstra et al. 2015; Simet et al. 2017; Melchior et al. 2017; Medezinski et al. 2018; Miyatake et al. 2018). Not surprisingly, as the statistical uncertainty continues to decrease, these systematics have come to dominate the total error budget (e.g. McClintock et al. 2018b).

In this work we combine cluster abundances and stacked weak

lensing mass measurements from the Sloan Digital Sky Survey data release 8 (SDSS DR8, Aihara et al. 2011) to simultaneously constrain cosmology and the richness–mass relation of galaxy clusters. Our cluster sample is selected using the red sequence Matched-filter Probabilistic Percolation algorithm (redMaPPer; Rykoff et al. 2014), and the stacked weak lensing mass estimates are presented in Simet et al. (2017). The analysis is similar in spirit to that of Rozo et al. (2010) but with significant updates, particularly with regards to the modeling of the cluster selection function. Our observables are the number of clusters and the mean cluster mass in bins of richness — our mass proxy — and redshift. We explicitly account for the small cosmological dependence of the recovered weak lensing masses in our analysis. To avoid confirmation bias, the bulk of the analysis has been performed blind: the values of the cosmological parameters sampled by the Monte Carlo Markov Chains (MCMC) were randomly displaced by an amount that was unknown to us, and were shifted back only after a broad set of validation tests were passed. No changes were done to the analysis pipeline post-unblinding. This is the first cosmology analysis to be performed blind in the cosmological parameters. The methods presented in this paper were developed for the forthcoming cosmological analysis of the DES Y1 redMaPPer cluster catalog (DES Collaboration in prep.).

This paper is organized as follows. In Section 2 we introduce the data used for this study. In Section 3 we present the model used to perform the cosmological analysis, including expectation values for the two observables, modeling of the systematics and likelihood model. We validate our model by means of synthetic data in Section 4. We detail our blinding procedure in Section 5. The results of our analysis are presented in Section 6 and 7. Finally we conclude in Section 8.

2 DATA

2.1 Cluster and Weak Lensing Catalogs

Both the cluster and weak lensing shear catalogs used in this analysis are based on the Sloan Digital Sky Survey data release 8 (SDSS DR8, Aihara et al. 2011). A summary of the data employed in this analysis is presented in Table 1. Throughout the paper, all masses are given in units of M_\odot/h , where $h = H_0/100 \text{ km s}^{-1} \text{ Mpc}^{-1}$, and refer to an overdensity of 200 with respect to the mean. We use "log" and "ln" to refer to the logarithm with base 10 and e respectively.

We use photometrically selected galaxy clusters identified in the SDSS DR8 with the redMaPPer cluster finding algorithm (Rykoff et al. 2014). In brief, redMaPPer utilizes all five bands (*ugriz*) of the SDSS imaging to self-calibrate a model for red-sequence galaxies. This model is then used to identify galaxy clusters as red galaxy overdensities, while simultaneously estimating the probability that each red galaxy is a cluster member. The cluster richness λ is the sum of the membership probabilities over all the red galaxies within an empirically calibrated scale radius, R_λ . Due to the probabilistic approach adopted by redMaPPer an individual galaxy can contribute to the richness of more than one cluster. We use the cluster richness λ as an observational mass-proxy in our analysis, calibrating the relation between galaxy richness and cluster mass using weak lensing data. Of the $\sim 14,000 \text{ deg}^2$ covered by SDSS DR8, we restrict ourselves to the $\sim 10,000 \text{ deg}^2$ of high quality contiguous imaging defined by the Baryon Oscillation Spectroscopic Survey (BOSS) experiment (Dawson et al. 2013). Typical

¹ <https://www.darkenergysurvey.org>

² <http://hsc.mtk.nao.ac.jp/sfp/>

³ <https://www.lsst.org/>

⁴ <http://sci.esa.int/euclid/>

⁵ <http://www.mpe.mpg.de/eROSITA>

Table 1. Summary of the data and systematic corrections adopted in the analysis. We use the same redshift range, $0.1 \leq z \leq 0.3$, for all the richness bins. The second column lists the observed number counts and their uncertainties, the latter estimated as the square root of the diagonal terms of the best-fit model covariance matrix (see Section 3.3). The numbers between parenthesis correspond to the number counts corrected for the miscentering bias factors listed in the third column (see Section 2.2). The values of the mean cluster mass reported here, $\log(\bar{M}_{200,m}^{\text{WL}})$, assume $\Omega_m = 0.30$; the two uncertainties shown correspond to the statistical and systematic error, respectively. We assume systematic errors to be fully correlated between the cluster bins. The fifth column lists the slopes which define the cosmological dependence of the weak lensing mass estimates (Eq. 1).

$\Delta\lambda^{\text{ob}}; z \in [0.1, 0.3]$	Number counts	γ^{Misc}	$\log(\bar{M}_{200,m}^{\text{WL}})[M_{\odot}/h]$	$d \log M^{\text{WL}}/d\Omega_m$
[20, 27.9)	3604 (3711) \pm 100	1.030 \pm 0.011	14.111 \pm 0.024 \pm 0.026	-0.65
[27.9, 37.6)	1740 (1788) \pm 61	1.028 \pm 0.011	14.263 \pm 0.030 \pm 0.024	-0.66
[37.6, 50.3)	942 (978) \pm 41	1.039 \pm 0.014	14.380 \pm 0.033 \pm 0.026	-0.68
[50.3, 69.3)	461 (476) \pm 27	1.034 \pm 0.015	14.609 \pm 0.036 \pm 0.028	-0.77
[69.3, 140)	217 (223) \pm 18	1.028 \pm 0.016	14.928 \pm 0.029 \pm 0.036	-0.65

photometric redshift uncertainties for SDSS redMaPPer clusters are $\sigma_z/(1+z) \lesssim 0.01$. We further restrict ourselves to the redshift range $z \in [0.1, 0.3]$. The lower redshift limit ensures that galaxies are sufficiently dim that the SDSS photometric pipeline produces reliable galaxy magnitudes, while the upper redshift limit is set by requiring that the cluster catalog be volume limited. We also apply a richness threshold $\lambda \geq 20$. In numerical simulations this richness threshold ensures that 99% of the redMaPPer galaxy clusters can be unambiguously mapped to individual dark matter halos (Farahi et al. 2016). In this work, we use v5.10 of the SDSS redMaPPer cluster catalog (Rozo et al. 2015).

The weak lensing mass estimates employed in this analysis are a slight update from those presented in Simet et al. (2017), and rely on the shear catalog presented in Reyes et al. (2012a). This catalog covers $\approx 9,000 \text{ deg}^2$ of the SDSS footprint and contains 39 million galaxies, corresponding to a source density of 1.2 gal/arcmin^2 . Shear estimates were derived from the SDSS imaging using the re-Gaussianization algorithm of Hirata & Seljak (2003) and the appropriately calibrated responsivity to convert the measured shape distortions into shear estimates. The multiplicative shear bias appropriate for this catalog was characterized in Mandelbaum et al. (2012) and Mandelbaum et al. (2013). In a recent work, Mandelbaum et al. (2017) revised the multiplicative shear estimate of this source catalog due to a previously undetected bias arising from the impact of neighboring galaxies and unrecognized blends. Our error budget accounts for this additional source of error. The photometric redshifts for the sources in the shear catalog were obtained using the Zurich Extragalactic Bayesian Redshift Analyzer (ZEBRA, Feldmann et al. 2006), and the associated systematic uncertainties were calibrated in Nakajima et al. (2012).

2.2 Cluster Number Counts Data

Following the weak lensing analysis of Simet et al. (2017), we collect our galaxy clusters in five richness bins and a single redshift bin (see Table 1). The richness limits of our bins are $\lambda^{\text{ob}} = [20, 27.9, 37.6, 50.3, 69.3, 140]$. The two key observational systematics in our analysis are photometric redshift errors and cluster miscentering. Photometric redshift uncertainties are forward-modeled as described in section 3.1.

Turning to cluster centering, in this work we assume that the correct center of a galaxy cluster is always coincident with a bright cluster galaxy (though not necessarily the brightest). This assumption is motivated by the fact that modern halo finders (e.g. Behroozi et al. 2013) define the center of dark matter halos as the position of the dominant dark matter substructure within the halo. It is ex-

pected that such a substructure will host a bright cluster galaxy, and therefore a proper comparison of theory to data should rely on identifying the correct central galaxy for each cluster. In redMaPPer, this is accomplished through an iteratively self-trained algorithm that combines luminosity and local galaxy density information to determine which cluster galaxy is the best central candidate in the cluster. This algorithm is demonstrably superior to centering clusters on the brightest cluster-member galaxy (Hikage et al. 2017). Nevertheless, miscentering systematics still arise from the fact that redMaPPer does not always successfully identify the correct central galaxy in each cluster. As we shall see shortly, the uncertainty in the systematic corrections due to cluster miscentering are very nearly negligible, so rather than incorporating these corrections into our forward-model, we have opted for the simpler route of applying a correction to the observed data-vector, and adding the corresponding systematic uncertainty in the abundances to the covariance matrix characterizing the uncertainty in our measurements.

Our miscentering correction is based on the analyses in Zhang et al. (in prep.) and von der Linden et al. (in prep.). To characterize the probability of a redMaPPer cluster being miscentered, we use subsamples of redMaPPer clusters with either *Chandra* or *Swift* X-ray imaging. Specifically, we compared the redMaPPer central galaxies to the X-ray derived cluster centers. Doing so, we demonstrated that $71.5\% \pm 6\%$ of redMaPPer galaxy clusters are correctly centered. This value is somewhat lower than but consistent with the estimate of Hikage et al. (2017) on the basis of the weak lensing profile of redMaPPer clusters. In addition, we also characterized the radial offset distribution of the miscentered clusters using a 2-dimensional Gaussian to describe the distribution of positional offsets for the miscentered clusters.

To determine the impact that cluster centering has on the recovered cluster richness, we measured the richness of all redMaPPer clusters at the location of the second most likely central galaxy, and characterized how cluster richness changes as a function of the centering offset. As expected, we find that miscentering systematically underestimates cluster richnesses, albeit with some scatter. Both the bias and scatter increase as the radial offset increases (Zhang et al., in prep.).

Having characterized (i) the fraction of miscentered clusters; (ii) the distribution of radial offsets of miscentered clusters; and (iii) how the richness of a cluster changes when it is miscentered by a given radial offset, we can readily estimate the impact of miscentering on the cluster abundance function. Specifically, we assigned richness values to halos in a numerical simulation using the model of Costanzi et al. (2018). The assigned halo richnesses are then scattered using our centering model. We compute the ra-

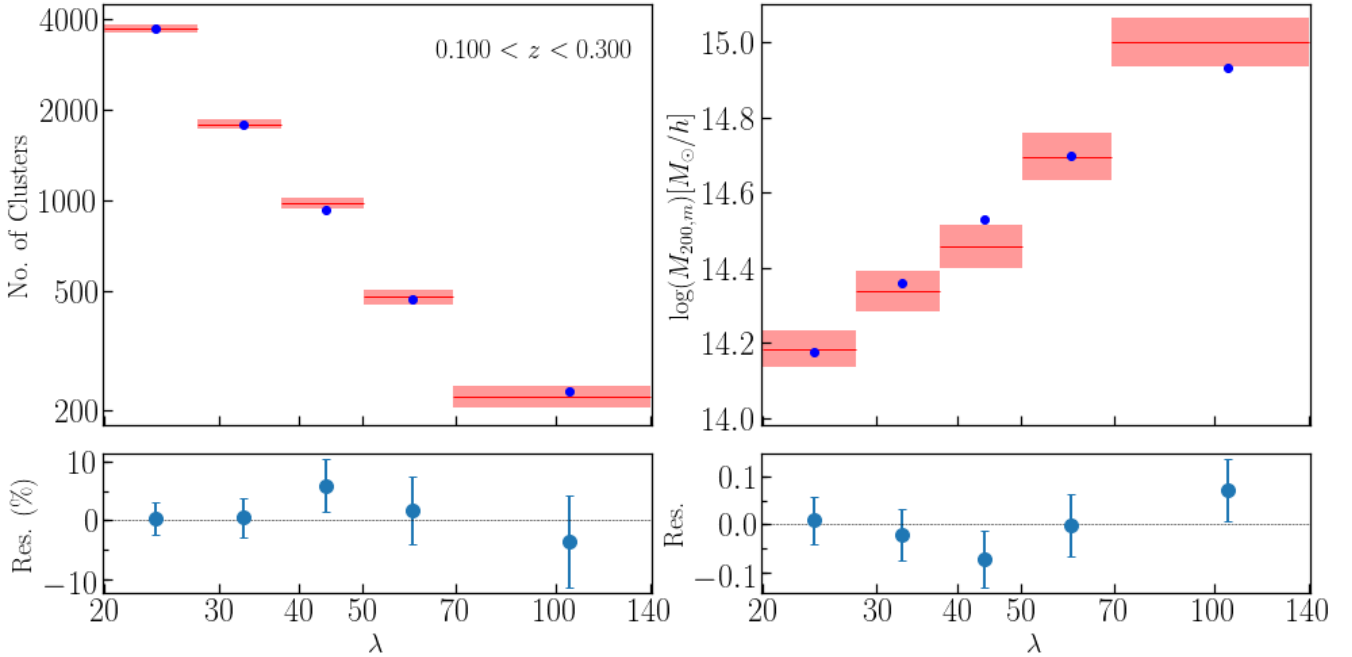


Figure 1. Observed (*shaded area*) and best-fit model (*dots*) of cluster number counts (*left panel*) and mean cluster masses (*right panel*) in the five richness bins considered. The model predictions have been computed as described in Section 3 using the best-fit values derived from our analysis. The y extent of the *shaded areas* is given by the square root of the diagonal terms of the corresponding covariance matrix. The lower panels show the percent residual (*left*) and the residual (*right*) of our best-fit model to the data.

ratio $\gamma^{\text{Misc}} = N^{\text{cent}}/N^{\text{miscent}}$ between N^{cen} , the number of clusters in a bin in the absence of miscentering, and N^{miscent} , the number of clusters in a bin including the impact of miscentering. We multiply the cluster abundance data vector by γ^{Misc} to correct for the impact of miscentering on the observed cluster abundances. From our Monte Carlo realizations, we are able to characterize both the mean correction and the corresponding covariance matrix. We apply the $\gamma^{\text{Misc}} \sim 1.030$ (see Table 1) systematic correction to the number of galaxy clusters we observe, and add the corresponding covariance matrix to the covariance matrix of the cluster counts. The uncertainty associated with cluster miscentering in the abundance function is $\approx 1.3\%$. That is, cluster miscentering is sub-dominant to Poisson noise in all richness bins. Its impact on the cosmological posterior is easily subdominant to the uncertainty in our calibration of the richness–mass relation.

The shaded regions in the top-left panel of Figure 1 shows the miscentering-corrected cluster abundances. The width of the regions along the y-axis is set by the diagonal entries of the corresponding covariance matrix, whereas their width along the x-axis reflects the width of the richness bin. Our best-fit model is shown as the blue points. The bottom-left panel shows the corresponding percent residuals.

2.3 Weak Lensing Cluster Masses

2.3.1 Measurement

We calculate the mean mass of clusters in a richness bin using the stacked weak lensing mass profiles of the clusters as described in Simet et al. (2017). These profiles are modeled using a Navarro, Frenk, and White profile (NFW, Navarro et al. 1997), accounting for the effects of cluster miscentering, halo triaxiality, and projec-

tion effects. The concentration of the best-fit NFW profiles is modeled using the mass-concentration relation presented in Diemer & Kravtsov (2015) with a free parameter for the amplitude.

In this work, we follow the methodology of Simet et al. (2017) to estimate the mean cluster mass in each bin with three critical exceptions:

(i) We correct for the $3\% \pm 3\%$ multiplicative shear bias due to undetected blends that was first identified in Mandelbaum et al. (2017). The original multiplicative bias in Simet et al. (2017) had a systematic uncertainty of $\pm 5\%$ (top-hat). To that we add a second bias term with a top-hat prior of width $3\% \pm 3\%$. The sense of the correction is to *increase* the recovered weak lensing masses. The standard deviation of the resulting distribution is 0.034, i.e. roughly equivalent to a 3.4% Gaussian scatter.

(ii) We update the centering priors employed in the weak lensing analysis based on the work of Zhang et al. and von der Linden et al. (in preparation). In Simet et al. (2017), the fraction of correctly centered galaxy clusters was estimated as $f = 80\% \pm 7\%$ on the basis of published X-ray data. The analyses in Zhang et al. and von der Linden et al. (in preparation) benefit from significantly improved statistics and custom X-ray analyses specifically designed to calibrate this source of systematic uncertainty. The revised fraction of correctly centered clusters is $f = 0.715 \pm 0.06$. The radial offset of miscentered clusters is described by a two dimensional Gaussian with width $\tau = (0.29 \pm 0.04)R_\lambda$, where R_λ is the cluster radius assigned by redMaPPer.

(iii) Rather than simultaneously modeling all galaxy clusters to derive a scaling relation that describes all richness bins, we estimate the mean mass of each individual richness bin. To account for the finite width of the bin, we fit a scaling relation to each individual bin, and then use the posterior of the scaling relation parameters to determine the mean cluster mass in that bin. It is these mean

cluster masses that we use as the weak lensing observables in our cosmological analysis.

The recovered mean mass in any single bin is only weakly dependent on the scatter assumed in the mass–richness relation when performing the fits. The degeneracy of the weak lensing posterior takes the form $\log\langle M|\lambda, \sigma \rangle = \log M + 0.06\sigma_{\ln M|\lambda}^2$. That is, varying $\sigma_{\ln M|\lambda}$ over the range [0.0, 0.5] modifies the recovered masses by an amount ranging from 0 to 0.015. We adopt a fiducial correction of 0.007 ± 0.007 . Following the analysis described in Simet et al. (2017, see section 5.5), we further estimate the systematic uncertainty in our weak lensing masses due to modeling the lensing profile with a pure NFW halo, without accounting for a two-halo term, or due to deviations from the NFW profile (e.g. Diemer & Kravtsov 2014). Briefly, we artificially populate dark matter halos in an N -body simulation by drawing from the richness–mass relation obtained by inverting our best fit mass–richness relation (Evrard et al. 2014). We then compute the corresponding cluster–mass correlation function, and project along the line of sight to obtain a predicted weak lensing profile, which we fit in the same way as we fit the data. The recovered biases for each of our richness bins varies from 2% on the low mass end to 3% on the high mass end. We apply these corrections to our data, and assign a systematic uncertainty on this correction equal to half the magnitude of the correction.

Our results are summarized in Table 1, where we collect the best weak lensing estimates for the mean mass of the galaxy clusters in each richness bin. The logarithm of the mean mass, $\log \bar{M}$, for each of our five richness bins is shown in the top-right panel of Figure 1, along with the best-fit model from our cosmological analysis. The bottom-right panel shows the corresponding residuals. We again emphasize that all aspects of this weak lensing analysis are as per Simet et al. (2017) except as detailed above; our results are a minor update to that work.

2.3.2 Weak Lensing Systematic Error Budget

Cluster cosmology has long been limited by systematic uncertainties in mass calibration. Here, we summarize the observational systematics we have explicitly accounted for in our analysis and their contributions to the error budget of the mass estimates. For further details on how these systematics were estimated, we refer the reader to Simet et al. (2017). Table 2 summarizes the sources of error detailed below.

- **Multiplicative shear and photo- z bias ($\pm 5\%$ top-hat).** This bias reflects the total multiplicative systematic uncertainty arising from two distinct sources of error, each contributing roughly the same amount of uncertainty: 1) systematic uncertainties in shear calibration as evaluated from realistic image simulations (Reyes et al. 2012b; Mandelbaum et al. 2012, 2013), and 2) photometric redshift systematics (Nakajima et al. 2012). This $\pm 5\%$ uncertainty is on the amplitude of the lensing profile. The equivalent mass error is obtained by multiplying by ≈ 1.3 , resulting in a $\pm 6.5\%$ top-hat error in the mass.⁶ In practice, the mass measurements are marginalized over the top-hat amplitude prior above.

⁶ The factor of 1.3 can be estimated by boosting a Navarro et al. (1997) profile by a constant factor, estimating the new R_{200m} aperture, and then verifying the ratio of the boosted mass to the original mass. The end result is that the boost to the mass is 1.3 times the boost to the profile.

- **Blending of lensing sources ($3\% \pm 3\%$ top hat).** This refers to the systematic bias introduced by the blending of sources discovered by Mandelbaum et al. (2017), and characterized using deep imaging from the Hyper-Suprime Camera. Again, the 3% uncertainty is in the correction of the amplitude of the profile, leading to a $\approx 1.3 \times 3\% = 3.9\%$ error in the mass.

- **Cluster triaxiality and projection effects (3%, Gaussian).** Cluster triaxiality and projection effects both introduce correlated cluster scatter between cluster richness and weak lensing masses. As detailed in Simet et al. (2017, section 5.3 and 5.4), we can readily compute the necessary corrections using the formalism laid out in Evrard et al. (2014). The estimate of the impact of triaxiality derived in this way is in excellent agreement with the simulation-based calibration of Dietrich et al. (2014). The quoted 3% error is the uncertainty in the mass.

- **Cluster centering ($\leq 1\%$).** Cluster centering is explicitly incorporated into the weak lensing mass estimates via forward modeling. The miscentering parameters have informative priors obtained from studies of the sub-sample of redMaPPer galaxy clusters with high-resolution X-ray data (Zhang et al. and von der Linden et al., in preparation). The weak lensing posterior fully accounts for the systematic uncertainty associated with cluster miscentering. The quoted 1% error is the uncertainty in the mass.

- **Modeling systematics ($\sim 2\%$, Gaussian, richness dependent).** Modeling systematics refers to biases in the inferred cluster mass due to our observational procedure. We explicitly calibrated this systematic using numerical simulations as detailed in the previous section. The quoted 2% error is the uncertainty in the mass.

- **Impact of the scatter on the recovered weak lensing masses (1.6%, Gaussian).** This error refers to the sensitivity of the weak lensing masses to the assumed scatter in the mass–richness relation detailed in section 2.3.1. The error ± 0.007 in $\log_{10} M$ corresponds to a 1.6% error on the mass.

- **Systematic uncertainty in the boost factor corrections (likely negligible).** Misidentification of cluster galaxies as lensing sources dilutes the lensing signal. However, these galaxies are obviously clustered around the cluster. Consequently, measurements of the source–cluster correlation function allow one to directly measure the contamination rate of the source galaxy population as a function of radius, and thus estimate the boost factor needed to correct the lensing signal. We explicitly checked that the statistical uncertainty associated with this measurement is negligible compared to the systematic errors in the multiplicative shear bias and photo- z corrections. However, small-scale features in the cluster or source selection function that are not adequately modeled by the associated random catalogs could lead to systematic uncertainties in the boost factor correction. Here, we assume these errors are negligible.

The total systematic error budget for our observational estimate of the mean mass of the galaxy clusters in a given richness bin is $\approx 6\%$ (Gaussian). Two additional, less well-understood potential systematics remain. These are:

- **Intrinsic alignments:** Radial alignments of member galaxies that are mistakenly selected as lensing sources will bias the corresponding cluster mass. Simet et al. (2017) derives a 6% upper limit for the impact of intrinsic alignments, but does not correct for this effect nor enlarge the systematic error budget since this intrinsic alignment signal has yet to be detected in the low-luminosity cluster member galaxies that can be potentially misidentified as lensing sources. Note intrinsic alignments are uni-directional: explicitly

modeling intrinsic alignments would increase the recovered cluster masses.

- Baryonic impact on the recovered cluster masses. In Simet et al. (2017) it is argued that baryonic effects were unlikely to have a large impact on the recovered cluster masses for two reasons. First, baryonic effects are strongest in the cluster core, which we exclude from our fits. Second, we do not impose priors on the amplitude and slope of the concentration–mass relation, allowing for the concentration to absorb the effects that baryons have on the cluster lensing profile, so long as an NFW profile remains a reasonable description of the halo profiles (Schaller et al. 2015). This hypothesis has received additional support from the work of Henson et al. (2017), who found that while baryonic physics can clearly impact the lensing profile of galaxy clusters, the bias incurred from fitting said profiles is independent of baryonic physics, provided the concentration–mass relation of the clusters is allowed to vary. Based on Figure 11 in that work, it is difficult to imagine baryonic effects introducing biases larger than $\approx 3\%$.

We do not increase our systematic error budget on the expectation that both of these effects will eventually be proven to be subdominant to the systematic errors quoted above. We are not aware of any unaccounted-for systematic effects impacting the recovered weak lensing masses at a level that exceeds that or is comparable to the systematics detailed above. A complete summary of the error budget associated with the weak lensing mass calibration of the SDSS redMaPPer clusters is detailed in Table 2.

2.3.3 Cosmology Dependence of the Recovered Masses

The weak lensing masses derived above depend on the angular diameter distance to the sources and the mean matter density at the redshift of the clusters. These in turn depend on cosmological parameters. Assuming a flat Λ CDM model, and using mass estimates in units of M_\odot/h , the only cosmological parameter that can appreciably impact the resulting weak lensing mass measurements is the matter density Ω_m . Consequently, we repeat our analysis along a grid of values for Ω_m ranging from $\Omega_m = 0.24$ to $\Omega_m = 0.36$ while setting $\Omega_\Lambda = 1 - \Omega_m$. As in Simet et al. (2017), we find the recovered log-masses scale as a linear function in the matter density Ω_m , i.e.

$$\log \bar{M}^{\text{WL}}(\Omega_m) = \log \bar{M}^{\text{WL}}|_{\Omega_m=0.3} + \left(\frac{d \log M^{\text{WL}}}{d \Omega_m} \right) (\Omega_m - 0.3) \quad (1)$$

The slopes derived from fitting Equation 1 to the data are listed in Table 1, and are used in our cosmological analysis to re-scale $\log \bar{M}^{\text{WL}}$ at each step of the MCMC by the appropriate Ω_m value.⁷

3 THEORY AND METHODS

In the previous section, we described how we constructed the observational vectors (cluster abundances and weak lensing masses) employed in our analysis. We now turn to describe how we model the expectation values of these observables and derive their covariance in order to simultaneously constrain both cosmology and the richness–mass relation of the redMaPPer clusters. In what follows, all quantities labeled with “ob” denote quantities inferred from

observation, while quantities labeled with “true” indicate intrinsic halo properties. $P(Y|X)$ denotes the conditional probability of Y given X .

3.1 Expectation values

3.1.1 Base Model

Let $\Delta\lambda_i^{\text{ob}}$ denote richness bin i , and Δz_j^{ob} denote the redshift bin j . The expectation value of the number of galaxy clusters $N(\Delta\lambda_i^{\text{ob}}, \Delta z_j^{\text{ob}})$ is given by

$$\langle N(\Delta\lambda_i^{\text{ob}}, \Delta z_j^{\text{ob}}) \rangle = \int_0^\infty dz^{\text{true}} \Omega_{\text{mask}}(z^{\text{true}}) \frac{dV}{dz^{\text{true}} d\Omega}(z^{\text{true}}) \times \langle n(\Delta\lambda_i^{\text{ob}}, z^{\text{true}}) \rangle \int_{\Delta z_j^{\text{ob}}} dz^{\text{ob}} P(z^{\text{ob}}|z^{\text{true}}, \Delta\lambda_i^{\text{ob}}), \quad (2)$$

where $dV/(dz^{\text{true}} d\Omega)$ is the comoving volume element per unit redshift and solid angle, and $\Omega_{\text{mask}}(z^{\text{true}})$ is the effective survey area at redshift z . The survey area depends on redshift because galaxy clusters are not point-like: whether a cluster is formally within the survey area or not depends not just on the location of the galaxy cluster in the sky, but also on how the survey boundaries (including star holes and any other masked regions) intersect the projected area of the cluster in the sky. To estimate the survey area, we randomly place clusters in the sky, and compute the fraction of the galaxy cluster that does not fall within the survey footprint. The footprint of the cluster survey is defined by the collection of all points for which at least 80 per cent of the cluster falls within the photometric survey boundaries. This 80% criterion is the fiducial choice for all redMaPPer runs, and is chosen as a compromise between requiring clusters not be heavily masked, and losing a minimal amount of area due to masking. In principle, this masking criteria implies that the survey area depends on cluster richness (via the scale radius R_λ), but we find this dependence to be negligible ($\leq 1\%$ over the redshift range $z \in [0.1, 0.3]$ employed in this study).

The second integral of Eq. 2 accounts for the uncertainty in the photometric redshift estimate. We model $P(z^{\text{ob}}|z^{\text{true}}, \Delta\lambda_i^{\text{ob}})$ — the probability of assigning to a cluster at redshift z^{true} a photometric redshift z^{ob} — with a Gaussian distribution having mean z^{true} and a redshift and richness-dependent variance. The variance is set by the reported photometric redshift uncertainty in the redMaPPer cluster catalog. Specifically, we fit a third-order polynomial to the redMaPPer photometric redshift errors as a function of redshift for galaxy clusters in each of our five richness bins (we find this is sufficient to fully describe our data). Photometric redshift uncertainties range from ≈ 0.005 at $z \approx 0.15$ to ≈ 0.014 at $z \approx 0.3$, with richer clusters having somewhat smaller photometric redshift uncertainties than low richness clusters.

As shown in Figure 9 of Rykoff et al. (2014), the redMaPPer photometric redshifts are excellent: they are nearly unbiased, and the reported photometric redshift uncertainties are both small and they accurately describe the width of the photometric redshift offsets relative to the spectroscopic cluster redshifts (where available). Using the specific cluster sample employed in this work ($\lambda \geq 20, z \in [0.1, 0.3]$), we evaluate the systematic bias of the redMaPPer photometric redshift by fitting a Gaussian distribution to the redshift offset $z_\lambda - z_{\text{spec}}$, where z_λ is our photometric cluster redshift estimate, and z_{spec} is the spectroscopic redshift of the central galaxy assigned to the cluster (when available). We find a mean bias of 0.002, i.e. $z_\lambda = z_{\text{spec}} + 0.002$. Likewise, from a Gaussian fit to the distribution of scaled errors $(z_\lambda - z_{\text{spec}})/\sigma_z$ we find

⁷ Our posterior extends to matter densities below $\Omega_m = 0.24$. We verified *a posteriori* that the linear matter density scaling extends to $\Omega_m = 0.15$.

Table 2. Error budget for the weak lensing mass calibration data used in our cosmological analysis. The ‘‘Gaussian equivalent’’ error for top-hat systematics refers to the square root of the variance of the top-hat prior of the appropriate effect. For instance, a Gaussian prior for shear and photo- z biases of $\pm 2.8\%$ has the same variance as a top-hat prior of $\pm 5\%$. The statistical error quoted in the table refers to the uncertainty in the amplitude of the mass–richness relation. The statistical uncertainty on any individual mass estimate is larger.

Source	Associated Error
Shear and Photo- z Bias	6.5% top-hat (3.8% Gaussian equivalent)
Source blending	3.9% top-hat (2.3% Gaussian equivalent)
Cluster triaxiality and projections	3% Gaussian
Cluster centering	$\leq 1\%$
Modeling systematics	2.0% Gaussian (richness dependent)
Scatter corrections	1.6% Gaussian
<hr/>	
Total Systematic Error	6.0% Gaussian
Statistical Error	4.8% Gaussian
<hr/>	
Total	7.7%

that the reported photometric redshift uncertainties in redMaPPer should be boosted by a factor of 1.014. In both cases, the statistical uncertainties in the estimates are negligible. We have verified that the above systematic errors are completely negligible by running two versions of our analysis, one without applying these corrections, and one after applying these corrections. The impact on the posteriors is negligible. For specificity, from here on out we apply the above corrections, that is, we set $\langle z^{\text{ob}}|z^{\text{true}} \rangle = z^{\text{true}} + 0.002$ and increase the photometric redshift errors by a factor of 1.014.

Finally, $\langle n(\Delta\lambda_i^{\text{ob}}, z^{\text{true}}) \rangle$ in Eq. 2 is the expected number density of halos in the richness bin $\Delta\lambda_i^{\text{ob}}$. This quantity is given by

$$\langle n(\Delta\lambda_i^{\text{ob}}, z^{\text{true}}) \rangle = \int_0^\infty dM n(M, z^{\text{true}}) \int_{\Delta\lambda_i^{\text{ob}}} d\lambda^{\text{ob}} P(\lambda^{\text{ob}}|M, z^{\text{true}}), \quad (3)$$

where $P(\lambda^{\text{ob}}|M, z^{\text{true}})$ denotes the probability that a halo of mass M at redshift z^{true} is observed with a richness λ^{ob} (see subsection 3.1.2) and $n(M, z^{\text{true}})$ is the halo mass function which is assumed to follow the form of Tinker et al. (2008):

$$n(M, z) = \frac{3}{4\pi R^3(M)} \frac{d \ln \sigma(M)^{-1}}{dM} f^{\text{Tinker}}(\sigma(M), z) \quad (4)$$

Several studies have explored how the mass function from N -body simulations should be extended in order to incorporate the effects of massive neutrinos (e.g. Brandbyge et al. 2010; Villaescusa-Navarro et al. 2014; Castorina et al. 2014; Liu et al. 2017). A common finding of these studies is that massive neutrinos play a negligible role in the collapse of dark matter halos, while they suppress the growth of matter density fluctuations on scales smaller than the neutrino free-streaming length. Here, we account for these effects following the prescription of Costanzi et al. (2013): (i) we neglect the density neutrino component in the relation between mass and scale — i.e. $M \propto (\rho_{\text{cdm}} + \rho_b)R^3$ — and (ii) use only the cold dark matter and baryon power spectrum components to compute the variance of the density field, $\sigma^2(M)$.

We can use similar arguments to the ones used to derive Eq. 2 to compute the expectation value for the mean mass of galaxy clusters within a specific richness and redshift bin. This is given by:

$$\langle \bar{M}(\Delta\lambda_i^{\text{ob}}, \Delta z_j^{\text{ob}}) \rangle = \left[\frac{\langle M^{\text{tot}}(\Delta\lambda_i^{\text{ob}}, \Delta z_j^{\text{ob}}) \rangle}{\langle N(\Delta\lambda_i^{\text{ob}}, \Delta z_j^{\text{ob}}) \rangle} \right], \quad (5)$$

i.e. the ratio of the expected total mass inside the bin over the total number of clusters inside said bin (Eq. 2). Note that observationally, we stack $\Delta\Sigma$, not M , and since the two are not linearly related

to each other — $\Delta\Sigma$ is proportional to the integrated mass density profile — it is not necessarily the case that the recovered weak lensing mass is identical to the mean mass of the clusters. However, as described in section 2.3.1, we calibrate the relation between the recovered weak lensing mass and the mean mass in a bin so as to ensure our measurement is an unbiased proxy of the mean mass of the clusters in a bin.

The total mass of all clusters in a bin is calculated via

$$\langle M^{\text{tot}}(\Delta\lambda_i^{\text{ob}}, \Delta z_j^{\text{ob}}) \rangle = \int_0^\infty dz^{\text{true}} \Omega_{\text{mask}} \frac{dV}{dz^{\text{true}} d\Omega}(z^{\text{true}}) \langle Mn(\Delta\lambda_i^{\text{ob}}, z^{\text{true}}) \rangle \int_{\Delta z_j^{\text{ob}}} dz^{\text{ob}} P(z^{\text{ob}}|z^{\text{true}}), \quad (6)$$

where the total mean mass per unit volume in the i -th richness bin is given by:

$$\langle Mn(\Delta\lambda_i^{\text{ob}}, z^{\text{true}}) \rangle = \int_0^\infty dM Mn(M, z^{\text{true}}) \int_{\Delta\lambda_i^{\text{ob}}} d\lambda^{\text{ob}} P(\lambda^{\text{ob}}|M, z^{\text{true}}). \quad (7)$$

In practice, the integrals over the observed redshift in the numerator and denominator of equation 5 are each weighted by the appropriate weak lensing weight per clusters $w_{\text{WL}}(z)$, where w is the mean weight applied to sources as a function of redshift — $w \propto \langle \Sigma_{\text{crit}}^{-1} \rangle^2 / (1+z)^2$ — times the number of sources per cluster. We have found including this weight changes the predicted masses by less than 1%. Nevertheless, our fiducial result includes this additional redshift weighting.

3.1.2 The Observed Richness–Mass Relation

Turning to the probability distribution $P(\lambda^{\text{ob}}|M, z^{\text{true}})$, in addition to the stochastic nature of the relation between cluster richness and halo mass, the observed richness of a galaxy cluster is subject to projection effects. Indeed, there are now multiple lines in support of the existence of projection effects in the SDSS redMaPPer cluster catalog (Farahi et al. 2016; Zu et al. 2017; Busch & White 2017; Sohn et al. 2017). Following Costanzi et al. (2018), we model $P(\lambda^{\text{ob}}|M, z^{\text{true}})$ as the convolution of two probability distributions:

$$P(\lambda^{\text{ob}}|M, z^{\text{true}}) = \int_0^\infty d\lambda^{\text{true}} P(\lambda^{\text{ob}}|\lambda^{\text{true}}, z^{\text{true}}) P(\lambda^{\text{true}}|M, z). \quad (8)$$

The first term inside the integral accounts for projection effects and observational noise in the richness estimates. The second term in-

side the integral accounts for the stochastic relation between halo mass and the intrinsic halo richness λ^{true} .

Below, we start describing the model adopted for the intrinsic richness–mass relation $P(\lambda^{\text{true}}|M, z)$. The probability distribution $P(\lambda^{\text{ob}}|\lambda^{\text{true}}, z^{\text{true}})$ was the focus of a detailed numerical study in a companion paper (Costanzi et al. 2018). A brief overview of that work is presented in the subsequent subsection.

The Intrinsic Richness–Mass Relation

Different parameterizations for $P(\lambda^{\text{true}}|M, z)$ have been proposed in the literature, typically assuming a log-normal distribution with the expectation value for the richness modeled as a power law (see e.g. Rozo et al. 2010; Mana et al. 2013; Murata et al. 2017). In this analysis we opt for a model which more closely resembles halo occupation distribution functions typically used to study galaxy clustering (Berlind & Weinberg 2002; Bullock et al. 2002). A recent review of halo occupation modeling and other approaches to modeling the galaxy–halo connection can be found in Wechsler & Tinker (2018) (see also e.g. the discussion in section 4 of Jiang & van den Bosch 2016 and Appendix D of Reddick et al. 2013). The total richness of a halo of mass M is given by $\lambda^{\text{true}} = \lambda^{\text{cen}} + \lambda^{\text{sat}}(M)$, where λ^{cen} is the number of central galaxies (either zero or unity), and λ^{sat} is the number of satellite galaxies in the cluster (Kraivtsov et al. 2004; Zheng et al. 2005). We model the expectation value of λ^{cen} as a simple step function, $\langle \lambda^{\text{cen}}|M \rangle = 1$ for $M \geq M_{\text{min}}$, and $\langle \lambda^{\text{cen}}|M \rangle = 0$ otherwise. While in practice these step functions have a finite width, we expect all clusters in our sample to have masses $M \gg M_{\text{min}}$, so that the step-function approximation should be easily sufficient.

Turning to the satellite galaxy population, it has long been known that the scatter in the number of satellites is super-Poissonian at large occupations numbers (Boylan-Kolchin et al. 2010), but is close to Poissonian otherwise. More recently, the number of satellites has been shown to be sub-Poissonian at very low occupancy (Mao et al. 2015; Jiang & van den Bosch 2016). Since we are interested in galaxy clusters, we ignore this small deviation from Poisson statistics at low N in our analysis. We add variance to a Poisson distribution by modeling $P(\lambda^{\text{sat}}|M)$ as the convolution of a Poisson distribution with a Gaussian distribution. Operationally, this is equivalent to assuming the number of satellite galaxies in a halo of mass M is a Poisson realization of some expectation value μ , where μ exhibits halo-to-halo scatter, e.g. due to formation history (Mao et al. 2015). We model the halo-to-halo scatter as a Gaussian with variance $\sqrt{\text{Var}(\mu)} = \sigma_{\text{intr}} \langle \lambda^{\text{sat}}|M \rangle$. This additional halo-to-halo scatter enables us to recover the super-Poisson scatter in the halo occupation at large occupancy numbers.

In detail, the expectation value of the satellite contribution to λ^{true} is given by (Kraivtsov et al. 2004; Zehavi et al. 2011)

$$\langle \lambda^{\text{sat}}|M \rangle = \left(\frac{M - M_{\text{min}}}{M_1 - M_{\text{min}}} \right)^\alpha, \quad (9)$$

Here, M_{min} is the minimum mass for a halo to form a central galaxy, while M_1 is the characteristic mass at which halos acquire one satellite galaxy. Our parameterization enforces $\langle \lambda^{\text{sat}}|M \rangle = 0$ when $M \leq M_{\text{min}}$. Finally, the expectation value of the Gaussian component is set to zero, while the variance of the Gaussian term is set to $\sigma_{\text{intr}} \langle \lambda^{\text{sat}}|M \rangle$.

The convolution of a Poisson distribution with a Gaussian distribution does not have an analytic closed form. However, we have found that a skew-normal distribution is an excellent approximation to the resulting distribution. Its model parameters — skewness and variance — depend on $\langle \lambda^{\text{sat}}|M \rangle$ and σ_{intr} , and are obtained by

fitting the skew-normal model to the appropriate Gaussian-Poisson convolution (see Appendix B). By creating a lookup table for these parameters, we can avoid having to numerically compute the convolution of the Poisson and Gaussian distributions, significantly increasing the computational efficiency of our model. In Section 6.2 we discuss how our choice of parameterization impacts the cosmological constraints derived from the SDSS redMaPPer sample.

Modeling Observational Scatter in Richness Estimates

The scatter in the distribution $P(\lambda^{\text{ob}}|\lambda^{\text{true}})$ is due to observational scatter, i.e. noise on the estimated richness values due to photometric noise, uncertainties in background subtraction, and projection effects. The latter refers to the boosting of the richness of a galaxy cluster due to additional galaxies along the line of sight that are mistakenly associated with the galaxy cluster. In Costanzi et al. (2018) we developed a formalism that quantitatively characterizes these effects, demonstrated the accuracy and precision of this formalism, and combined it with numerical simulations to calibrate the impact of projection effects and observational noise in the SDSS DR8 redMaPPer catalog. Here, we provide a succinct description of that work, and refer the reader to Costanzi et al. (2018) for details.

The scatter in λ^{ob} due to background subtraction and photometric noise in the data is estimated as follows. First, we inject synthetic clusters of known richness λ^{true} and redshift z^{true} at a random position in the survey footprint. We then measure the recovered richness, and repeat the procedure 10,000 times to characterize the associated scatter. The scatter is decomposed into a Gaussian component — the observational noise — and a decaying exponential component that characterizes the tail of high richness clusters due to projection effects. The biases in the recovered richness, as well as the standard deviation of the Gaussian component, are recorded. It is this Gaussian distribution that we use to model observational noise.

The tail due to projection effects is modeled explicitly as a sum over the true richnesses of galaxy clusters along the line of sight, weighted by a “projection kernel” that is calibrated directly from the data. The validity of this model is explicitly demonstrated by comparing the impact of projection effects around random points in the data to the impact of projection effects we predict when applying our model to N -body simulations (see also §4). Having validated the model, we measure the impact of projection effects at the location of massive halos in the N -body simulations, and use this calibrated measurement to characterize the tail due to projections arising from correlated large structures.

The end result of this procedure is a calibrated model for $P(\lambda^{\text{ob}}|\lambda^{\text{true}})$ composed of a Gaussian observational noise, an exponentially decaying noise contribution due to projection effects, and a tail that extends to $\lambda^{\text{ob}} = 0$ which accounts for incompleteness due to percolation effects: low-richness clusters along the same line of sight of a richer objects can lose some of their galaxies to the richer object, leading to a severe underestimation for their richness. Figure 2 shows the distribution $P(\lambda^{\text{ob}}|\lambda^{\text{true}})$ as a function of λ^{true} at redshift $z = 0.2$. The inset shows a cross-section of the distribution for $\lambda^{\text{true}} = 25$. The three main components of the distribution are obvious by eye: a Gaussian kernel due to observational noise, a large tail to high richness due to projection effects, and a low-richness tail due to percolation effects.

We note that the calibration of $P(\lambda^{\text{ob}}|\lambda^{\text{true}})$ depends on the input cosmology and richness–mass relation parameters adopted to generate the synthetic cluster catalog. However, we verified in Costanzi et al. (2018) that this assumption has no impact on the

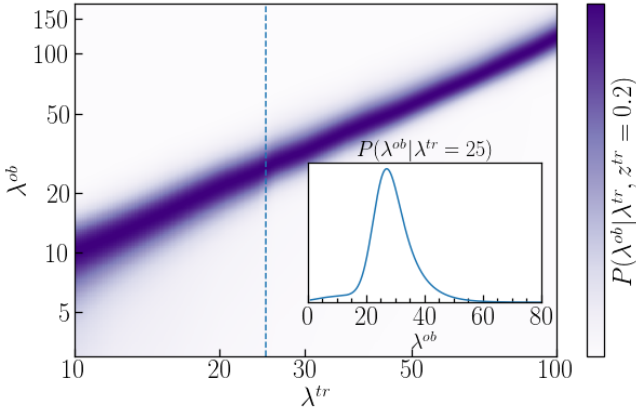


Figure 2. $P(\lambda^{\text{ob}}|\lambda^{\text{true}})$ as a function of the *true* richness at redshift $z = 0.2$. The inset shows a section of $P(\lambda^{\text{ob}}|\lambda^{\text{true}})$ for $\lambda^{\text{true}} = 25$ (dashed line in the main plot). Note the non-Gaussian tail to high richness due to projection effects, and the low-richness tail due to percolation effects.

posterior of the cosmological parameters. In section 6 we explicitly test the robustness of our cosmological constraints to different calibrations of $P(\lambda^{\text{ob}}|\lambda^{\text{true}})$.

3.2 Mass-Function Systematics

The modeling of the cluster counts and mean cluster masses depends on the halo mass function. Here, we use the Tinker et al. (2008) halo mass function. Tinker et al. (2008) report their mass function formula to be accurate at the $\approx 5\%$ level, but we do not have a robust estimate of the associated systematic uncertainty as a function of mass. Moreover, a number of studies comparing different halo finders and fitting functions suggest a systematic uncertainty of the order of 10% (e.g. Knebe et al. 2013; Hoffmann et al. 2015; Despali et al. 2016). To characterize the systematic uncertainty in the halo mass function in dark matter only simulations we introduce two nuisance parameters q and s relating the Tinker et al. (2008) mass function to the true mass function via

$$n(M, z) = n(M, z)^{\text{Tinker}} (s \log(M/M^*) + q), \quad (10)$$

where the pivot mass is set to $\log(M^*) = 13.8 h^{-1} M_{\odot}$. Note that if $q = 1$ and $s = 0$, then the halo mass function is given by the Tinker et al. (2008) formula. We set the priors on q and s using the ensemble of simulations developed as part of the Aemulus project (DeRose et al. 2018). This is a set of 40 N -body simulations spanning a range of cosmologies in the redshift range $0.0 < z < 1.0$. Each simulation box has a length $L = 1050 h^{-1}$ Mpc and contains 1400^3 particles. The particle mass is cosmology dependent, and averages $\approx 3.5 \times 10^{10} h^{-1} M_{\odot}$. The cosmologies sampled by the simulation spans the 4σ confidence interval from WMAP (Hinshaw et al. 2013) and *Planck* (Planck Collaboration et al. 2016a) in combination with Baryon Acoustic Oscillation data (Anderson et al. 2014) and the Union 2.1 Super-Nova (SN) data (Suzuki et al. 2012). Halo catalogs were generated using the ROCKSTAR algorithm (Behroozi et al. 2013). Further details of the simulation data as well as the convergence tests done to ensure the reliability of these simulations are presented in DeRose et al. (2018).

We fit the simulation halo abundance data for the nuisance parameters s and q at each snapshot of each of the 40 simulations by computing the ratio $n^{\text{Sims}}(M, z)/n(M, z)^{\text{Tinker}}$. Next, we model the distribution of (s, q) values as Gaussian, and fit for the mean values

and covariance matrix describing the scatter of (s, q) across all 320 snapshots. We find $\bar{s} = 0.037$ and $\bar{q} = 1.008$, with a covariance matrix:

$$\mathcal{C}(\bar{s}, \bar{q}) = \begin{bmatrix} 0.00019 & 0.00024 \\ 0.00024 & 0.00038 \end{bmatrix}. \quad (11)$$

The above matrix is the sum of the covariance matrix obtained from the fit of s and q , i.e. the statistical calibration uncertainty in the mean values of the parameters, and the covariance matrix describing the simulation-to-simulation scatter in s and q . That is, the above covariance matrix fully accounts for any possible deviations of the Tinker et al. (2008) halo mass function to the test set of 40 N -body simulations employed here. Note too the variance of q corresponds to a 6% uncertainty in the amplitude of the halo mass function, consistent with the quoted precision in Tinker et al. (2008). The above covariance matrix and best fit values define the bivariate Gaussian priors used for the parameters s and q in our cosmological analysis. Future analyses should benefit from the significantly higher precision that can be achieved using emulators (e.g. McClintock et al. 2018a).

The above analysis does *not* account for the impact of baryons on the halo mass function. Several recent works have estimated the impact of baryonic feedback on total masses of halos and, thereby, the mass function (e.g. Cui et al. 2014; Velliscig et al. 2014; Bocquet et al. 2016; Springel et al. 2017). These works all find that baryonic impact decreases with increasing radial aperture. For the specific mass definition we adopt, namely a 200 overdensity criterion relative to mean, the impact of AGN-based full physics is modest for massive ($M \gtrsim 10^{14} h^{-1} M_{\odot}$) halos. In the IllustrisTNG simulation, full physics leads to a mean enhancement of $\sim 3\%$ while multiple methods analyzed by Cui et al. (2014) produce mainly decrements in M_{200c} of roughly similar magnitude. Due to the current uncertainty in modeling baryonic effects, we defer its inclusion into the error budget of the halo mass function to future work. For now, we simply note that a 3% systematic uncertainty in the halo mass function is already sub-dominant to the precision of the Tinker mass function, as characterized by our model parameters s and q .

3.3 Covariance Matrix

Having specified the expectation values for our observables (cf. Section 3.1) we need to define the covariance matrix of our data vector in order to fully specify the likelihood function. Here, we assume that the abundance and weak lensing data are uncorrelated. This assumption is well justified: the weak lensing error budget is strongly dominated by shape noise, and the dominant systematic is the overall multiplicative shear and photo- z bias of the source catalog. None of these errors affect the abundance data, and are therefore clearly uncorrelated.

Our Gaussian likelihood model takes the form

$$\mathcal{L}(\mathbf{d}|\boldsymbol{\theta}) \propto \frac{\exp\left[-\frac{1}{2}(\mathbf{d} - \mathbf{m}(\boldsymbol{\theta}))^T \mathbf{C}^{-1}(\mathbf{d} - \mathbf{m}(\boldsymbol{\theta}))\right]}{\sqrt{(2\pi)^M \det(\mathbf{C})}}. \quad (12)$$

where \mathbf{C} is the total covariance matrix detailed below, and \mathbf{d} and $\mathbf{m}(\boldsymbol{\theta})$ are respectively the data vectors (see Table 1) and the expectation values for the number counts and $\log M$ (Equation 2 and 5, respectively).

In reality, the likelihood for the abundance data is a convolution of a Poisson error on the counts and a Gaussian error due to density fluctuations within the survey area (e.g. Hu & Cohn 2006; Takada & Spergel 2014). Such a convolution does not have

an analytic closed form. Here, we take care to ensure that all of our richness bins are well populated — our least populated richness bin contains over 200 galaxy clusters — so that the Poisson component can be adequately modeled with a Gaussian distribution. Consequently, our likelihood for the abundance data can be modeled as a Gaussian with a total covariance matrix having three distinct contributions:

- (i) A Poisson contribution due to the Poisson fluctuation in the number of halos at given mass in the survey volume.
- (ii) A sample variance contribution due to the fluctuations of the density field in the survey volume.
- (iii) A contribution due to uncertainty in the miscentering corrections detailed in section 2.2.

The Poisson and sample variance contributions to the covariance matrix are computed analytically at each step of the chain to properly account for their dependence on cosmology and model parameters. At high richness, the Poisson contribution dominates, with sample variance becoming increasingly important at low richness (Hu & Kravtsov 2003). The analytical expression used to derive these two terms is provided in Appendix A, and it is validated by means of mock catalogs. In particular, we use the mock cluster catalogs generated by Costanzi et al. (2018) to calculate the variance in the abundance for each of the richness bins employed in our analysis. To do so, we split the full simulated survey area into N patches, ranging from $N = 100$ to $N = 900$, and use these patches to estimate the variance within the survey using a Jackknife method. Note that jackknife methods cannot adequately resolve modes that are larger than the jackknife region under consideration. Consequently, for the purposes of comparing our analytic estimates to the jackknife covariance matrix, we truncate our sample variance estimates by setting matter power spectrum to zero below the wavenumber $k_{\min} = \pi/R_{\max,N}$, where $R_{\max,N}$ is the radius of a spherical volume equal to the volume of the jackknife patch considered (see Eq. A5). As we can see from Figure 3, our analytic estimates are a good match to the observed variance in the simulations. We have also explicitly verified using our synthetic cluster catalog that the sample variance contribution to the mean cluster mass is negligible relative to the statistical and systematic uncertainties of the weak lensing analysis. We also find that the cross-correlation between number counts and the mean weak lensing cluster mass obtained from our jackknife estimates is consistent with zero.

Turning to the uncertainty in the weak lensing mass estimates, we use the posteriors from the stacked weak lensing analysis described in Section 2.3 (see Table 1). Critically, these posteriors are found to be nearly Gaussian in the log, that is, the posterior is well described by a log-normal distribution. Consequently, we model the weak lensing likelihood as a Gaussian distribution in $\log M$. The errors include not just the statistical uncertainty of the measurement, but also systematic uncertainties due to shear and photo- z biases (multiplicative shear bias), cluster projections, halo triaxiality, and miscentering effects. The overall shear and photo- z multiplicative bias is shared across all richness bins. Consequently, the variance associated with this error should be perfectly correlated across all bins.

To determine the overall mass error in each bin associated with the multiplicative bias we proceed as in Melchior et al. (2017, section 5.7) and McClintock et al. (2018a, section 5.6). First, we repeat our weak lensing analysis while fixing the systematic parameters. We then subtract the variance obtained from these fixed-bias run to the total variance measured while floating the multiplicative bias parameters. The resulting variance is the variance attributable to the

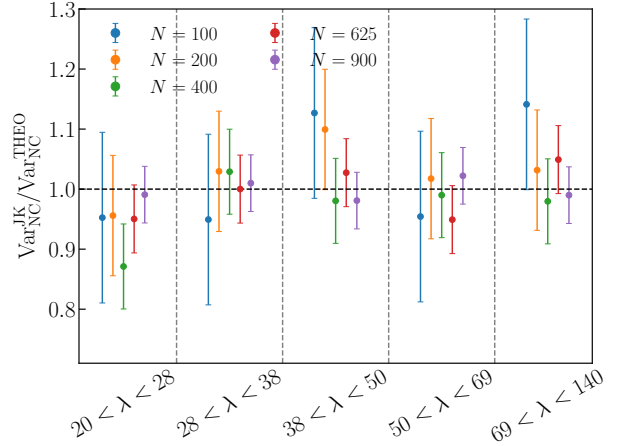


Figure 3. Comparison between the analytically derived variance for the number counts and the one derived from the mock catalog. Different colors correspond to the different splitting schemes used to estimate the Jackknife covariance matrix. Error bars are estimated from the jackknife covariance matrices itself assuming the jackknife realizations to be Gaussian distributed.

multiplicative bias. We do this for all five richness bins, and verify that, as expected, the variance due to multiplicative bias corrections to the $\Delta\Sigma$ profile, σ_b^2 , is nearly richness-independent, and roughly consistent with the expectation $\sigma_{\ln M} \approx 1.3\sigma_b$. The systematic uncertainty on the log of the masses is $\sigma_{\log M} = 0.026$. This value is larger than the 0.023 systematic quoted in Simet et al. (2017) because of the new contribution to the systematic error budget from blended sources, and the scatter correction. The error is perfectly correlated across all richness bins, so we set $C_{ij} = 0.026^2$ along the non-diagonal elements of the covariance matrix. This corresponds to the 6% total systematic error in Table 2. The diagonal entries of the covariance matrix are taken directly from the posteriors of our weak lensing analysis (see Simet et al. (2017) for details). Finally, as noted in Section 2.3, using numerical simulations we estimated that our fitting procedure introduces a bias that varies from 2% at low richness to 3% at high richness. We adopt a systematic uncertainty in this correction equal to half the magnitude of the correction, and add this (sub-dominant) contribution to arrive at the final covariance matrix employed for the weak lensing data.

In summary, our likelihood:

- Is Gaussian in the abundances, and includes Poisson, sample variance, and miscentering uncertainties.
- Is Log-normal in the weak lensing masses, as per the posteriors of Simet et al. (2017). It also accounts for the covariance due to shared multiplicative shear and photo- z biases, blended sources, and cluster triaxiality and projection effects. These systematics are assumed to be perfectly correlated across all richness bins.
- Has no covariance between the abundance and weak lensing data. We expect this to be an excellent approximation.

The posteriors from our analysis are fully marginalized over all sources of systematic uncertainty described above.

4 VALIDATION TESTS

We validate our likelihood framework by placing cosmological constraints from a synthetic cluster catalog whose cosmology and

richness–mass relation is known a priori. The mock data are generated starting from an N -body simulation run with 1400^3 dark matter particles in a box of comoving size $L = 1050\text{Mpc } h^{-1}$. The code used is L-Gadget, a variant of Gadget (Springel 2005). The simulation assumes a flat- Λ CDM model with $\Omega_m = 0.286$, $h = 0.7$, $\Omega_b = 0.047$, $n_s = 0.96$, and $\sigma_8 = 0.82$. Lightcone data, including a halo catalog down to $M_{200m} = 10^{12.5} h^{-1} M_\odot$, is constructed from the simulation on the fly. The halo finder is ROCKSTAR (Behroozi et al. 2013). For further details, see DeRose et al, in preparation; this is one realization of the L1 box described in that work.

We build a synthetic cluster catalog as follows. First, each halo is assigned a richness λ^{true} drawn from the $P(\lambda^{\text{true}}|M, z)$ distribution detailed in Section 3.1. We set our fiducial model parameters to: $\alpha = 0.704$, $\log M_{\text{min}} = 11.0$, $\log M_1 = 12.12$ and $\sigma_{\ln \lambda} = 0.25$. These fiducial values have been chosen by inverting the mass–richness relation of Simet et al. (2017) to arrive at parameters for the richness–mass relation (Eq. 9). The assigned richnesses are then modified to account for observational noise plus projection effects as described in Costanzi et al. (2018). Specifically:

(i) Starting at the richest halo, we compute the projected richness of each halo via

$$\lambda_i^{\text{ob}} = \lambda_i^{\text{true}} + \sum_{j \neq i}^N \lambda_j^{\text{true}} f_{ij}^A w(\Delta z_{ij}, z_j). \quad (13)$$

Here, the index j runs over all $j \neq i$ clusters, f_{ij}^A is the fraction of the area of the j -th object which overlaps with the i -th cluster, and $w(\Delta z_{ij}, z_j)$ is the data-calibrated weight which accounts for the redshift distance between the cluster i and j .

(ii) A Gaussian noise is added to the projected richness to account for observational errors (including the effects of background subtraction).

(iii) Having calculated the observed projected richness of the richest galaxy cluster, we update the richnesses of all remaining clusters via

$$\lambda_j^{\text{true}} = \lambda_j^{\text{ob}} (1 - f_{ij}^A w(\Delta z_{ij}, z_j)). \quad (14)$$

That is, the richness of cluster j is reduced by the amount it contributed to the richest cluster.

(iv) We now move on to the next richest cluster in the catalog, and iterate the above procedure to compute the observed projected richness of every halo in the simulation.

(v) Finally, we assign a photometric redshift to every cluster based on their spectroscopic redshifts using the model in section 3.1.

Given our synthetic cluster catalog, we now compute our observable data vectors. The cluster counts are measured using the same binning scheme as for the real data (see Table 1). As for the synthetic weak lensing masses, these are obtained from the mean halo mass in each richness bin. We also add a log-normal noise to the mean weak lensing masses by drawing from the covariance matrix described in Section 3.3. To mimic the fact that the weak lensing masses are estimated assuming $\Omega_m = 0.3$ while the simulation use the fiducial value $\Omega_m = 0.286$, we invert Equation 1 to arrive to our final mock data vector:

$$\log \bar{M}^{\text{WLMOCK}} = \log \bar{M}^{\text{WL}} \Big|_{\Omega_m=0.286} - \left(\frac{d \log M^{\text{WL}}}{d \Omega_m} \right) (0.286 - 0.3)$$

Figure 4 shows the constraints obtained by analyzing one realization of our synthetic data set with our pipeline. This analysis varies the same parameters and assumes the same priors as the real

data analysis (see Section 6). We can see that our analysis successfully recovers the true values of the parameters of our synthetic data set (red lines in the triangle plots). Because this test relied on a single simulation, we could not use it to validate the width of our posteriors.

5 BLINDING AND UNBLINDING

In order to avoid confirmation biases our cosmological analysis was performed blinded. By “blinded”, we mean that the following protocols were followed:

(i) The cosmological parameters in the MCMC were randomly displaced before being stored, and the random displacement was stored in binary (i.e. a not-human-readable format).

(ii) All modeling choices — specifically which set of cosmological models and models for the scaling relations we would consider — were made before unblinding. In this work, we chose to focus exclusively on flat Λ CDM cosmologies with massive neutrinos. Our choice to let neutrino mass vary follows the practice of the DES Year 1 combined probe analysis (DES Collaboration et al. 2017a).

(iii) The set of scaling relation models considered in our analysis was fully specified before unblinding. In addition to our fiducial model for the scaling relation, we considered three additional sets of models for the scaling relation (see Figure 8). “Random-point-injection” refers to the $P(\lambda^{\text{ob}}|\lambda^{\text{true}})$ distribution calibrated by inserting galaxy clusters at random locations in the sky, i.e. neglecting the contribution from correlated structures to the observed richness. Since we know this model underestimates projection effects, we take half the difference between our fiducial model and the “Random-point-injection” model as our estimate of the systematic uncertainty in our cosmological posteriors. We further tested how allowing the intrinsic scatter of the richness–mass relation to scale with mass affected our cosmological posterior constraints. Finally, to compare to existing works, we considered both a power-law scaling relation with constant scatter and a scaling relation modeled after the work of Murata et al. (2017).

(iv) All priors were set before unblinding.

(v) The set of external data sets we would compare against was decided before unblinding. Here, we distinguish between data sets with which we intend to combine our analysis and further test the flat Λ CDM model (see next item), and other large-scale-structure data sets that constrain the $S_8 \equiv \sigma_8(\Omega_m/0.3)^{1/2}$ parameter. For the latter, we simply compare the recovered S_8 values, rather than test for consistency across the full parameter space. Specifically, we compare our S_8 constraints to those of *Planck* (Planck Collaboration et al. 2016a)⁸, the DES Year 1 3x2 point analysis (DES Collaboration et al. 2017a), the KiDS-450+2dFLenS analysis (Joudaki et al. 2018), and the KiDS-450+GAMA analysis (van Uitert et al. 2018). In addition, we compare our constraint to several additional recent cluster abundance constraints, namely those from the *Planck*-SZ catalog (Planck Collaboration et al. 2016b), those from the South Pole Telescope (de Haan et al. 2016) and Atacama Cosmology Telescope (Hasselfield et al. 2013), and those from the Weighing the Giants team (Mantz et al. 2015). Finally, we compare

⁸ After we unblind our analysis new *Planck* results have been released (Planck Collaboration et al. 2018). To provide the most updated results we decided to consider the latest *Planck* constraints (hereafter *Planck* DR18) as CMB data set to compare against the SDSS clusters results.

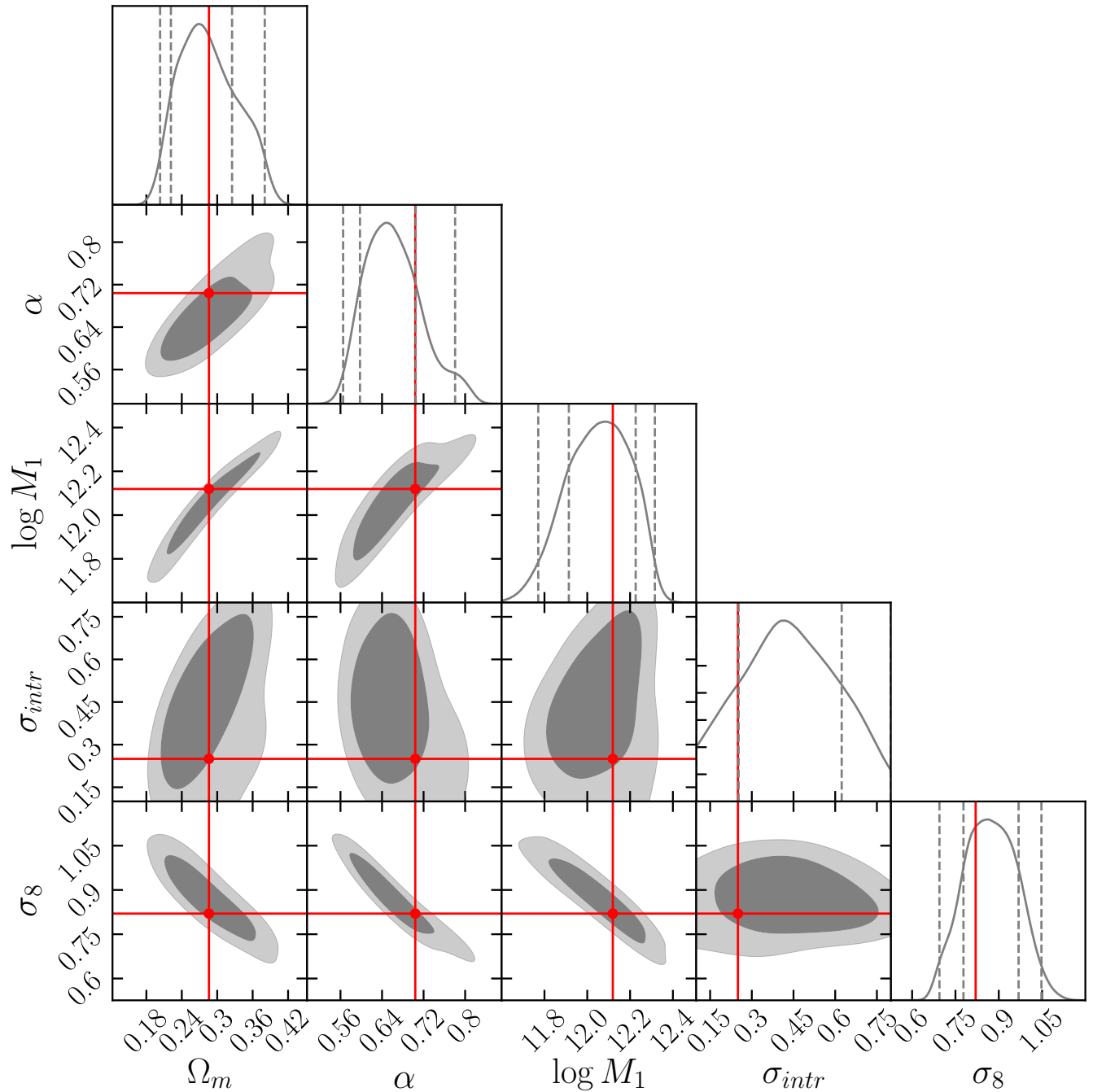


Figure 4. 68% and 95% confidence contours obtained running our pipeline on mock data. The input parameter values used to generate the simulation and the mock data catalog are shown in *red*. The *dashed* lines shown in the 1-d marginalized distributions (diagonal of the triangle plot) correspond to the 0.025, 0.16, 0.84 and 0.975 quantiles of the distributions. Not included in this plot is the parameter M_{\min} , which is prior dominated.

our constraints to those derived from the SDSS maxBCG cluster sample (Rozo et al. 2010). For these purposes, we consider analyses *A* and *B* to be consistent if their central values of S_8 deviate by no more than $3\sigma_{\text{tot}}$, where $\sigma_{\text{tot}}^2 = \sigma_A^2 + \sigma_B^2$.

(vi) The set of external data sets with which we intend to combine with the SDSS analysis (provided the two are deemed to be consistent, see metrics for consistency below) were fully specified. In addition to *Planck* (Planck Collaboration et al. 2016a), we decided to compare our constraints to those derived from Baryon

Acoustic Oscillations (BAO) as measured in the 6dF galaxy survey (Beutler et al. 2011), the SDSS Data Release 7 Main Galaxy sample (Ross et al. 2015), and the BOSS Data Release 12 (Alam et al. 2017). As for the *Planck* constraints, we relied on the TT+lowP data set. With the expectation that our combined BAO and cluster abundance analysis (which included a prior on $\Omega_b h^2$) would result in a tight constraint on the Hubble constant (see e.g. DES Collaboration et al. 2017b), we also planned on comparing our posterior in h to that of Riess et al. (2016).

(vii) The metrics for consistency with external data sets were selected before unblinding. Specifically, consistency between two data sets A and B was established by testing whether the hypothesis $\mathbf{p}_A - \mathbf{p}_B = 0$ is acceptable (see method ‘3’ in Charnock et al. 2017). Here \mathbf{p}_A and \mathbf{p}_B are the model parameters of interest as constrained by data sets A and B respectively. The two data sets were deemed to be consistent if the point $\mathbf{p}_A - \mathbf{p}_B = 0$ falls within the 99% confidence level of the multi-dimensional distribution of $\mathbf{p}_A - \mathbf{p}_B$. If two data sets were found to be inconsistent with one another, we did not consider the combined analysis. We note that in order for this test to be the sharpest possible test, it is important to restrict one-self to parameter sub-spaces that are well constrained in both data sets. To that end, in all cases we restrict the parameter space for comparison to the set of parameters whose posterior is at most half as uncertain as the prior of each individual data set.

(viii) No comparison of our cosmological constraints to any other data sets were performed prior to unblinding.

The weak lensing analysis upon which our work relies was not performed blind (Simet et al. 2017), though our forthcoming analysis using data from the Dark Energy Survey data will have benefited from a blind weak lensing analysis. Importantly, all relevant weak lensing priors — specifically the multiplicative shear bias, photometric redshift correction, source dilution, etc — were finalized well before the advent of our particular analysis: no tuning of any input catalog was done in response to the weak lensing analysis of Simet et al. (2017) or our own cosmological analysis.

During the DES internal review process the question arose whether past experiences from people in our team — particularly those involved with the development of the maxBCG cluster catalog (Koester et al. 2007) — had in any way informed the development of redMaPPer, possibly leading to unintended biases in this way. The redMaPPer algorithm was *not* tuned based on previous experiences. The algorithm iteratively self-trains the colors of red-sequence galaxies as a function of redshift without any cosmological assumptions. The parameters chosen for the richness estimation — particularly the aperture used — were selected by minimizing the scatter in X-ray luminosity at fixed richness (Rykoff et al. 2012). We do adopt a fiducial cosmology when defining our richness measurements (this is necessary to turn physical apertures into angular apertures), but since the richness–mass relation is not known a priori, it carries no cosmological information.

Our unblinding protocol was defined by the set of requirements detailed below.

(i) Our inference pipeline had to successfully recover the input cosmology in a synthetic data set. For details, see Section 4.

(ii) All SDSS-only chains (including alternative models) were run demanding the fulfillment of the Gelman-Rubin criteria (Gelman & Rubin 1992) with $R - 1 \leq 0.03$ being our convergence criteria.

(iii) We had to demonstrate systematics uncertainties in our model for $P(\lambda^{\text{ob}}|\lambda^{\text{true}}, z)$ did not appreciably bias our cosmological posteriors. Since the random-point-injection model for this distribution is an extreme model, we adopted half of the systematic shift in the values of the cosmological parameters between our fiducial model and this extreme model as our estimate of the associated systematic uncertainty. Note this definition implies that the extreme random-point-injection model is consistent with our fiducial model at 2σ despite being clearly extreme. We demanded that these systematic shifts be less than the corresponding statistical uncertainties.

(iv) We explicitly verified that the priors of all parameters which

we expected would be well-constrained a priori are not informative, that is the posteriors of such parameters did not run into the priors within the 95% confidence region. In case this condition was not fulfilled we planned to extend the relevant prior ranges until the requirement was met. Parameters that are prior dominated (i.e. their posterior runs into the prior) are M_{min} , σ_{intr} , s , q , h , $\Omega_b h^2$, $\Omega_\nu h^2$, and n_s . All of these were expected to be prior dominated a priori, and all prior ranges were purposely conservative. Of these, the two that might be most surprising to the reader are M_{min} and σ_{intr} , as these parameters help govern the richness–mass relation. However, notice that M_{min} is the mass at which halos begin to host a single central galaxy; since our cluster sample is defined with the richness threshold $\lambda \geq 20$, the mass regime of halos which host a single galaxy is not probed by our data set. Likewise, our data vector is comprised only of the mean mass of galaxy clusters in a given richness bin, a quantity that is essentially independent of the scatter in the richness–mass relation (see McClintock et al. 2018b).

(v) The χ^2 of the data for our best-fit model must be acceptable. To this end we considered the best-fit χ^2 distribution recovered from 100 mock data realizations generated from the best-fit model of the data. We assumed these 100 trials were distributed according to a χ^2 distribution, and fit for the effective number of degrees of freedom. The number of degrees of freedom is not obvious a priori due to the presence of priors in the analysis. We considered the χ^2 of our data to be not acceptable if the probability to exceed the observed value was less than 1%, after marginalization over the posterior for the effective number of degrees of freedom. We emphasize that verifying an acceptable χ^2 does not unblind the cosmological parameters. While our model did indeed have an acceptable χ^2 (see section 6.1 for details), our plan was to revisit our model and covariance matrix estimation procedures in the case of an unacceptable χ^2 value. This proved unnecessary.

(vi) Finally, this paper underwent internal review by the collaboration prior to unblinding. All members of the DES cluster working group, as well as all internal reviewers, agreed that our analysis was ready to unblind before we proceeded.

After all of our unblinding requirements were satisfied, we proceeded to unblind our analysis. No changes to the analyses were made post unblinding.

6 RESULTS

6.1 SDSS Cluster Abundances and Weak Lensing Data

We model the abundance of galaxy clusters and their weak lensing masses assuming a flat Λ CDM cosmological model, allowing for massive neutrinos. The full set of cosmological parameters we consider is: $\ln(10^{10} A_s)$, Ω_m , n_s , $\Omega_b h^2$, h , and $\Omega_\nu h^2$. Neutrinos are included assuming three degenerate neutrino species. We adopt the same priors as in the DES Year 1 analysis of galaxy clustering and weak lensing (DES Collaboration et al. 2017a), with the exception of h , where we adopt the slightly more restrictive prior $h = 0.7 \pm 0.1$. There are also two parameters (s and q) associated with systematic uncertainties in the halo mass function, and 4 parameters governing the richness–mass relation: M_{min} , M_1 , α , and σ_{intr} . The priors for all parameters are summarized in Table 3. We have explicitly verified that increasing the range of the priors adopted for the richness–mass relation parameters does not adversely impact the recovered cosmological constraints.

The result of our MCMC fitting procedure is shown in Figure 5, while the marginalized posterior values are reported in Table 3.

Table 3. Model parameters and parameter constraints from the joint analysis of redMaPPer SDSS cluster abundance and weak lensing mass estimates. In the fourth column we report our model priors: a range indicates a top-hat prior, while $\mathcal{N}(\mu, \sigma)$ stands for a Gaussian prior with mean μ and variance σ^2 . In the fifth column are listed the maximum likelihood values of the 1-d marginalized posterior along with the $1\text{-}\sigma$ errors. Parameters without a quoted value are those having marginalized posterior distribution corresponding to their prior. Note that systematic uncertainties in the lensing masses are contained in their covariance, and are therefore not explicitly modeled in the likelihood. For the priors on the nuisance parameters s and q we report here only the square root of the diagonal terms of the covariance matrix defined in Equation 11. The distribution characterizing the impact of observational noise, projection effects, and percolation includes several additional parameters that are held fixed. The systematic uncertainty associated with uncertainties in these parameters is estimated by repeating our analysis using an extreme set of values for these parameters, as estimated using random clusters in the SDSS (Costanzi et al. 2018). Because these parameters are not marginalized over in our chains, they are not included in this table. We stress that the impact of the associated systematic error is negligible relative to the recovered width of our cosmological posteriors.

Parameter	Description	Prior	Posterior
Ω_m	Mean matter density	[0.0, 1.0]	$0.22^{+0.05}_{-0.04}$
$\ln(10^{10} A_s)$	Amplitude of the primordial curvature perturbations	[-3.0, 7.0]	$3.97^{+0.67}_{-0.47}$
σ_8	Amplitude of the matter power spectrum	–	$0.91^{+0.11}_{-0.10}$
$S_8 = \sigma_8(\Omega_m/0.3)^{0.5}$	Cluster normalization condition	–	$0.79^{+0.05}_{-0.04}$
$\log M_{min} [M_\odot/h]$	Minimum halo mass to form a central galaxy	(10.0, 14.0)	11.2 ± 0.2
$\log M_1 [M_\odot/h]$	Characteristic halo mass to acquire one satellite galaxy	$[10M_{min}, 30M_{min}]$	$12.42^{+0.16}_{-0.13}$
α	Power-law index of the richness–mass relation	[0.4, 1.2]	$0.65^{+0.05}_{-0.07}$
σ_{intr}	Intrinsic scatter of the richness–mass relation	[0.1, 0.8]	< 0.4
s	Slope correction to the halo mass function	$\mathcal{N}(0.037, 0.014)$	–
q	Amplitude correction to the halo mass function	$\mathcal{N}(1.008, 0.019)$	–
h	Hubble rate	$\mathcal{N}(0.7, 0.1)$	–
$\Omega_b h^2$	Baryon density	$\mathcal{N}(0.02208, 0.00052)$	–
$\Omega_\nu h^2$	Energy density in massive neutrinos	[0.0006, 0.01]	–
n_s	Spectral index	[0.87, 1.07]	–

Parameters not shown in Figure 5 and without a quoted posterior in Table 3 are those whose posterior is equal to their prior. Also shown in the table is the posterior for the so-called cluster normalization condition parameter $S_8 \equiv \sigma_8(\Omega_m/0.3)^{0.5}$. In practice, the σ_8 – Ω_m degeneracy in our cosmology analysis corresponds to

$$\sigma_8 \left(\frac{\Omega_m}{0.3} \right)^{0.47} = 0.80 \pm 0.04. \quad (15)$$

Nevertheless, unless otherwise specified in the text, from this point on we will focus on the cluster normalization condition $S_8 \equiv \sigma_8(\Omega_m/0.3)^{0.5}$ as it has become a standard parameter in the literature.

A comparison of our best-fit model with the data is shown in Figure 1. The χ^2 of our best-fit model is $\chi^2 = 5.71$. To assess the goodness of the fit we generated 100 mock data vectors from our best-fit model of the data and, for each of them, we recovered the best-fit χ^2 value. Assuming a χ^2 distribution for the 100 trials we fit for the effective number of degree of freedom, finding $\nu_{\text{eff}} = 7.56 \pm 0.37$ (see Figure 6). This corresponds to a probability to exceed of $p = 0.64 \pm 0.04$. Thus, we conclude that our model provides a good fit to the data.

We wish to determine whether the error budget in the cosmological parameter S_8 is dominated by uncertainties in the abundance data or the weak lensing data. To determine this, we first compute the predicted abundance and weak lensing data using our best-fit model. We then run two additional chains using the predicted expectation values as a synthetic data vector. The key difference between the two chains is that for one we reduce the abundance covariance matrix by a factor of 100, while for the other chain we reduce the covariance matrix of the weak lensing data by a factor of 100. By comparing the cosmological posteriors for these two chains we can determine if there is one observable which dominates our error budget. In both cases the corresponding poste-

rior on S_8 have an error bar $\sigma_{S_8} = 0.03$ (see *left* panels of Figure 7). Thus we conclude that our error budget on cosmological parameters is not dominated by either of the uncertainties associated with the two observables. Rather, both observables contribute in comparable ways to the total error budget of S_8 .

The balance between weak lensing errors and abundance uncertainties is surprising in light of the fact that all analyses to date have been dominated by uncertainties in the calibration of the mean of the observable–mass relation. Nevertheless, this feature of our results can be easily understood. The *left* panel of Figure 7 demonstrates that there is a strong degeneracy between S_8 and σ_{intr} . Unlike previous analysis, which have incorporated well-motivated simulation-based priors on the scatter of the observable–mass relation, our analysis adopts a very broad prior on the scatter of the richness–mass relation. This broad prior reflects the difficulty inherent to predicting properties of the richness–mass relation a priori. Since the scatter parameter impacts the detailed shape of the abundance function — larger scatter leads to flatter abundance functions — exquisitely precise measurements of the abundance function can break the degeneracy between scatter and S_8 , leading to significant improvements in the S_8 constraints. Conversely, even modest constraints of the scatter parameter σ_{intr} can break the S_8 – σ_{intr} degeneracy, leading to tighter constraints.

We demonstrate the impact that a modestly-precise prior can have on our cosmological posteriors by redoing our analysis while imposing a flat prior $\sigma_{intr} \in [0.1 : 0.3]$. The corresponding posterior for S_8 is $S_8 = 0.77 \pm 0.03$. If we now repeat our sensitivity analysis, and shrink the weak lensing mass errors, the width of the S_8 posterior decreases to $\sigma_{S_8} = 0.01$, while decreasing the abundance errors while holding the weak lensing errors fixed has a negligible impact on the posterior. These trends are illustrated in the *right* panel of Figure 7. Evidently, external constraints on the

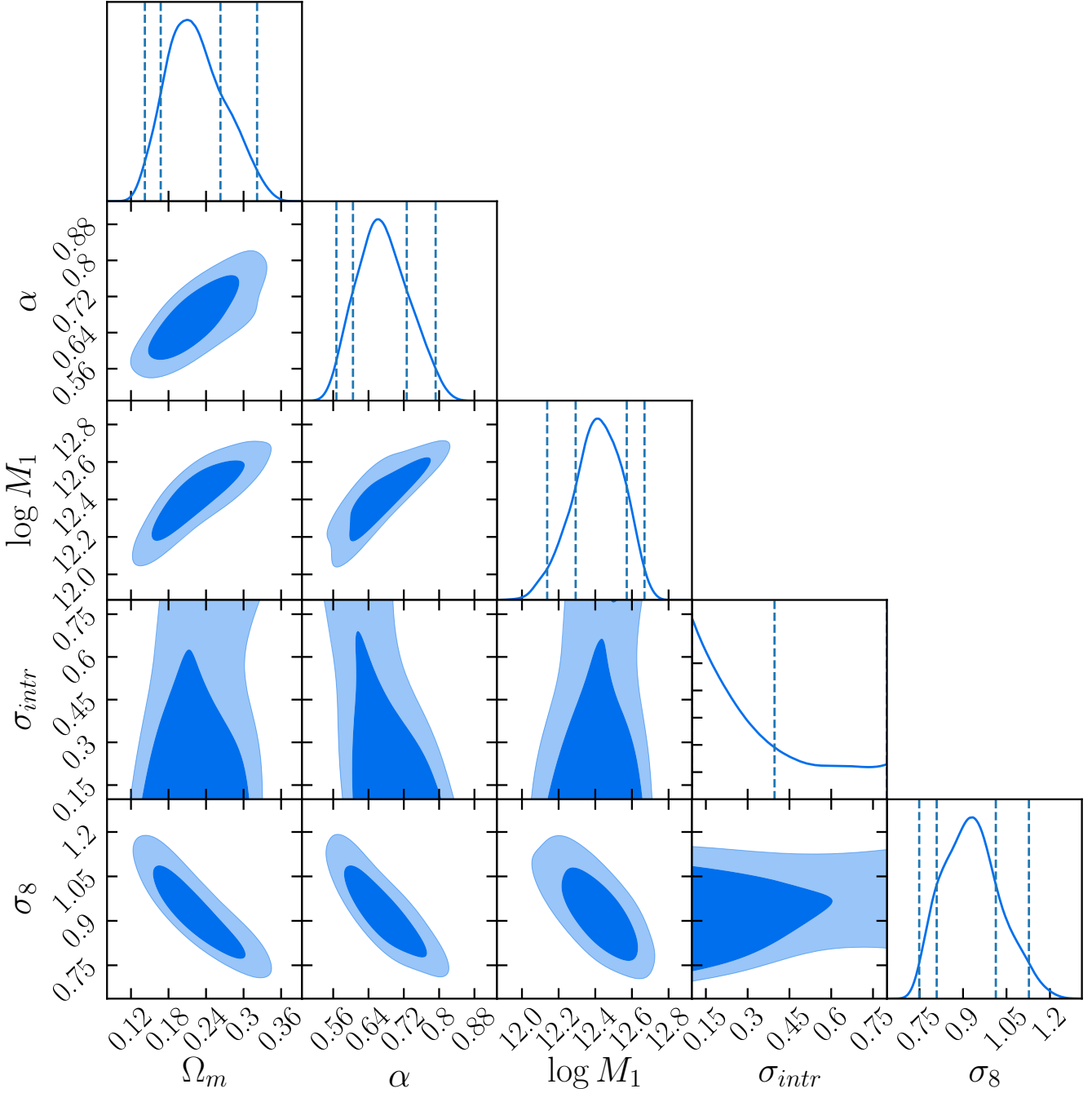


Figure 5. Marginalized posterior distributions of the fitted parameter. The 2D contours correspond to the 68% and 95% confidence levels of the marginalized posterior distribution. The dashed lines on the diagonal plots correspond respectively to the 2.5th, 16th, 84th and 97.5th percentile of the 1-d posterior distributions. The description of the model parameters along with their posterior are listed in Table 1. Not included in this plot is the parameter M_{\min} , which is prior dominated.

scatter of the richness–mass relation of redMaPPer clusters are extremely valuable from a cosmological perspective.

6.2 Robustness to Assumptions About the Richness–Mass Relation

Figure 5 shows that there is strong covariance between cosmological parameters and parameters governing the richness–mass relation.

Consequently, it is of critical importance to simultaneously fit for the richness–mass relation as part of the cosmological analysis. Likewise, one may ask to what extent are our cosmological constraints sensitive to the detailed assumptions we have made about the richness–mass relation. To address this question, we have repeated our analysis with a range of richness–mass relation models as summarized in Figure 8. The models considered are:

- A model that allows for the intrinsic scatter σ_{intr} to vary with

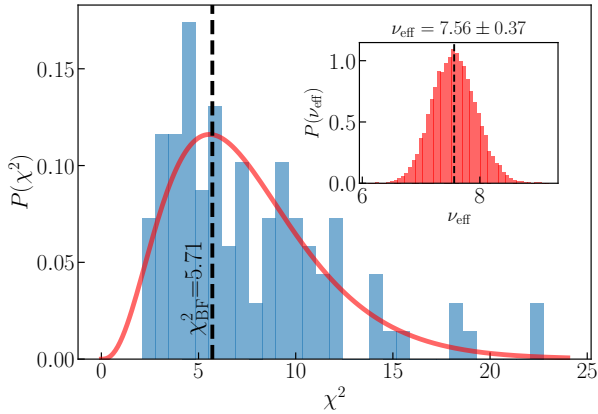


Figure 6. Goodness of fit analysis. The *blue* histogram shows the distribution of the best-fit χ^2 values recovered from 100 mock data realizations generated from the best-fit model of the data. The *red* histogram in the inset plot shows the posterior distribution for the effective number of degrees of freedom obtained by fitting a χ^2 distribution to the above 100 χ^2 values. The *red solid* line represents the χ^2 distribution for the best-fit model ($\nu_{\text{eff}} = 7.56$), while the vertical *dashed* line corresponds to the χ^2 value of the data.

mass via

$$\sigma_{\text{intr}}(M) = \sigma_{\text{intr},0} (M / (M_1 - M_{\text{min}}))^{\beta}. \quad (16)$$

- A model that neglects the perturbations on the observed richness due to correlated structures. To this end we set $P(\lambda^{\text{ob}} | \lambda^{\text{true}}, z^{\text{true}})$ equal to the probability distributions recovered from injecting synthetic clusters at random positions in the survey mask. This calibration provides a very strict lower limit on the scatter of λ^{ob} due to projection effects: clusters do contain correlated large scale structure. The difference in the posteriors of the cosmological parameters between our fiducial run and the random-point-injection model places a strict upper limit on the systematic associated with our modeling of projection effects.

- A model in which the richness–mass relation is a simple power law — $\langle \lambda^{\text{true}} | M \rangle = \lambda_0 (M / 10^{14.344})^{\alpha}$ — and $P(\lambda^{\text{true}} | M)$ is a log-normal distribution in which the total scatter is the sum of a Poisson-like term and an intrinsic scatter term — $\sigma_{\text{intr}}^2 = \sigma_{\text{intr}}^2 + ((\lambda^{\text{true}} | M) - 1) / (\lambda^{\text{true}} | M)^2$.

- The richness–mass relation model of Murata et al. (2017). This model assumes $P(\lambda^{\text{ob}} | M)$ is log-normal, the mean richness–mass relation is a power-law, and the intrinsic scatter is mass-dependent, and given by $\sigma_{\text{intr}}(M) = \sigma_{\text{intr},0} + \beta \ln(M / 2.2 \times 10^{14})$. According to Murata et al. (2017) all integrals are truncated at $M_{\text{min}} = 10^{12} h^{-1} M_{\odot}$. Reassuringly, when we mirror the analysis of Murata et al. (2017) and fix our cosmological parameters to Planck Collaboration et al. (2016a) we reproduce their results despite significant methodological differences in how the weak lensing data is incorporated into the likelihood.

As can be seen in Figure 8 our cosmological posteriors are all consistent with one another. It is clear that the more restrictive parameterizations (e.g. log-normal + power-law) result in somewhat tighter constraints. Notably, our standard result — which we believe is the most appropriate model — results in the most conservative posteriors. In particular, we see that opening up the freedom of a mass–dependent intrinsic scatter does not negatively impact the posterior on S_8 . Interestingly, we noticed that our random-point injection model, which grossly underestimates the impact of

projection effects, had a small impact on the posterior of the intrinsic scatter, modifying instead the best fit value for the slope of the richness–mass relation, a degeneracy that should be easily broken via multi-wavelength analyses of the redMaPPer clusters. Finally, we note that the Murata-like parameterization has the largest impact on our posteriors, with the systematic shift in S_8 being comparable to the width of the posterior. We will address the origin of this shift in the next section.

6.3 The Observable–Mass Relation for redMaPPer Clusters

The left panel of Figure 9 shows the observed richness–mass relation $\langle \lambda^{\text{ob}} | M \rangle$ for our fiducial model at the mean sample redshift $z = 0.22$. The error bars reflect the posterior of the mean relation at each mass. These are computed as follows: for each point in our chains we evaluate $\langle \lambda^{\text{ob}} | M \rangle$ along a grid of masses. The mean and variance of $\langle \lambda^{\text{ob}} | M \rangle$ across the chain are then recorded. In the left panel of Figure 9 we use these quantities to plot the 68% confidence interval for the posterior of the mean of the richness–mass relation. The central panel of Figure 9 is computed in a similar way, only now we show the posterior for the scatter $\text{Var}^{1/2}(\lambda^{\text{ob}} | M)$.⁹

For comparison we include in the two panels the richness–mass relation and scatter derived in Murata et al. (2017), who analyzed this sample of clusters using the same weak lensing shear catalog we employed. There are significant methodological differences between the two analyses. Specifically, Murata et al. (2017):

- Uses emulators instead of an analytic model for the weak lensing profile of clusters, effectively holding the concentration of the galaxy clusters fixed. They also place no priors on the miscentering parameters.
- Adopts a log-normal model for $P(\lambda^{\text{ob}} | M)$.
- Adopts a power-law relation for both the mean and variance of λ^{ob} at fixed mass.

The *yellow* bands in Figure 9 are obtained by estimating the 68% confidence region of their posterior from 10,000 Gaussian random draws of the richness–mass relation parameters quoted in Murata et al. (2017). Despite methodological differences, the two results are remarkably similar over the mass range probed by the survey ($M \gtrsim 10^{13.5} [M_{\odot} / h]$, see below). It is especially impressive how well the scatter found in Murata et al. (2017) agrees with our finding, confirming their argument that the mass-trend in the scatter of the richness–mass relation they recovered is due to contamination from projection effects.

There is, however, one notable difference between our results and those of Murata et al. (2017). Figure 7 of Murata et al. (2017) shows that the mass distribution for clusters in the richness bin $\lambda^{\text{ob}} \in [20, 30]$ extends to masses as low as $10^{12} h^{-1} M_{\odot}$, the mass cut imposed in that analysis. Figure 10 shows the posterior of the

⁹ A reader might find useful to have simple power-law fits to the data shown in Figure 9. We provide such fits below:

$$\begin{aligned} \langle \lambda^{\text{ob}} | M \rangle &= 30.0 \left(\frac{M}{3 \times 10^{14} [M_{\odot} h^{-1}]} \right)^{0.75} \\ \text{Var}^{1/2}(\lambda^{\text{ob}} | M) &= 14.7 \left(\frac{M}{3 \times 10^{14} [M_{\odot} h^{-1}]} \right)^{0.54}. \end{aligned}$$

The fits correspond to the best fit-relations. No errors are provided since these are meant to be “quick-look” references. Detailed quantitative analyses should rely on the full posterior of our model, which will be made available at <http://risa.stanford.edu/redmapper/> when the paper is published.

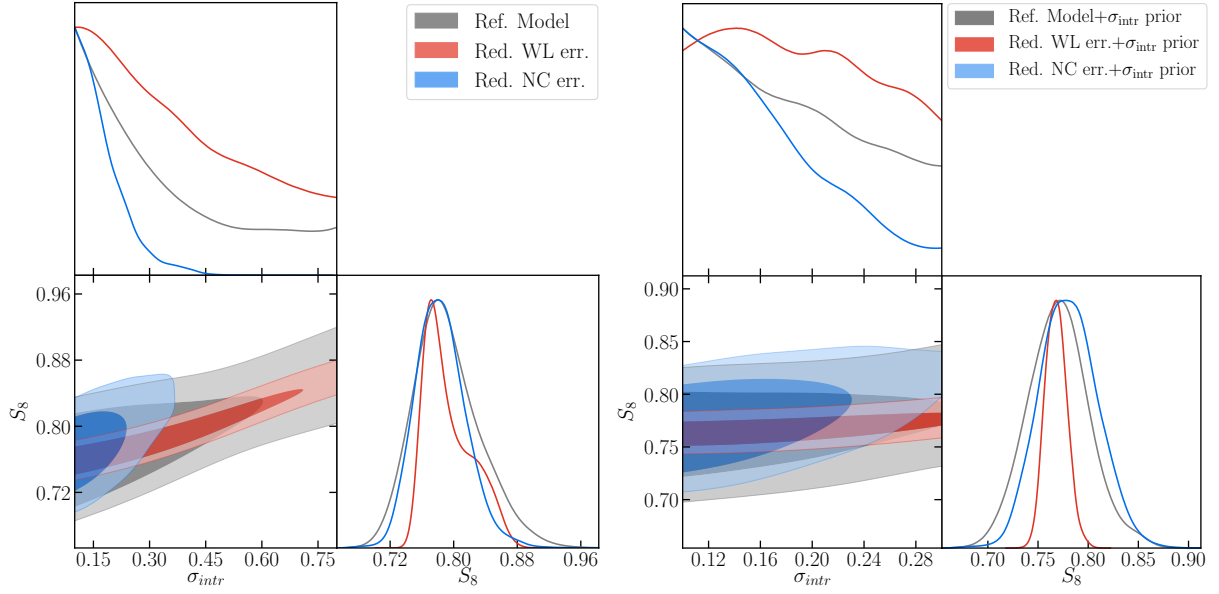


Figure 7. Assessment of the error budget on S_8 associated with our two observables: cluster abundance data and weak lensing mass estimates. *Left panels:* Comparison of the $(S_8, \sigma_{\text{intr}})$ constraints derived in our reference model (*gray* contours) and rescaling the weak lensing data (*red* contours) or the number counts (*blue* contours) covariance matrix by a factor 0.01. *Right panels:* same as the left panels but including a flat prior on the scatter parameter: $\sigma_{\text{intr}} \in [0.1 : 0.3]$. See text for additional details and discussion.

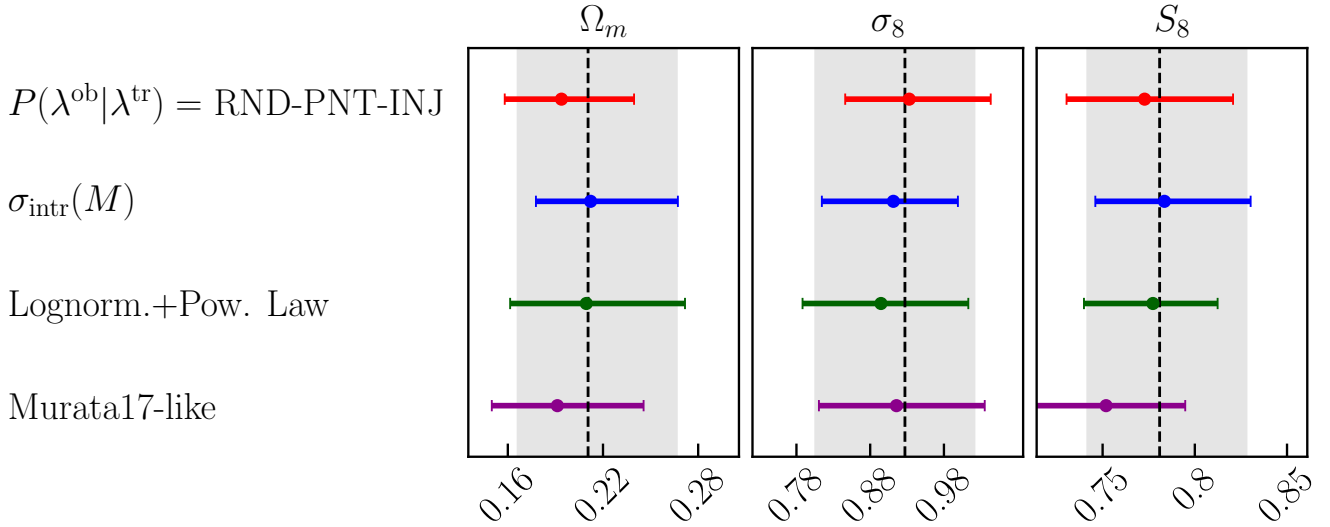


Figure 8. Comparison of the 68% confidence regions for Ω_m , σ_8 and S_8 derived assuming different model for $P(\lambda^{\text{ob}}|M)$ (see Section 6.2). The shaded area corresponds to the constraints derived using our reference model.

mass distribution for clusters in our analysis, as labeled. Unlike Murata et al. (2017), we do not see any evidence for a population of low-mass ($M \leq 10^{13} h^{-1} M_{\odot}$) clusters. We believe the large number of low-mass halos in the Murata et al. (2017) analysis is driven by the combination of a log-normal model whose scatter increases with decreasing mass, and a model that ignores the central/satellite dichotomy at low masses. Our model avoids this problem by: 1) enforcing the appropriate Poisson limit in the limit of low λ^{true} ; and 2) developing a simulation-based model for projection effects that adequately characterizes non-Gaussian tails in the distribution $P(\lambda^{\text{ob}}|\lambda^{\text{true}})$.

As an independent check of our conclusions, we estimate the halo masses of individual redMaPPer clusters using the stellar content of the redMaPPer central galaxy. Specifically, we fit the photometric SDSS data using a stellar population synthesis model to derive the stellar mass of each of the assigned redMaPPer central galaxies (Moustakas et al., in preparation). We then use the UniverseMachine algorithm (Behroozi et al. 2018) to determine the relation between the stellar mass of the central galaxy of a halo and the mass of the parent halo. Using the relation between halo mass and the stellar mass of the central galaxy, we can readily assign a mass estimate to each redMaPPer cluster. We find that the stellar

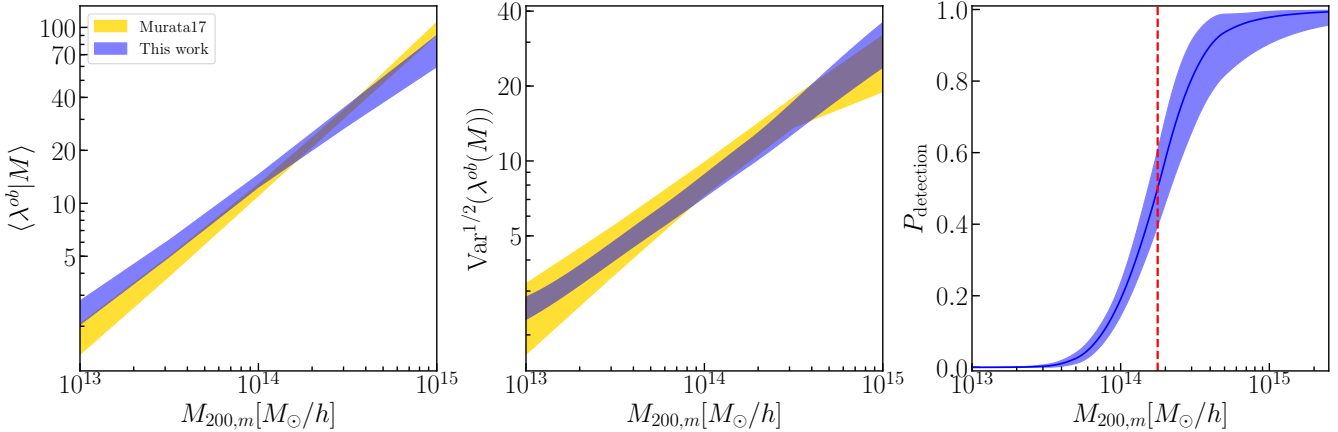


Figure 9. Observable–mass relation and mass-selection function of the redMaPPer catalog assuming our reference richness–mass relation model (Eq. 9) at the mean sample redshift $z = 0.22$. *Left* panel: Expectation value for the observed richness as a function of mass. *Central* panel: Scatter of $\lambda^{ob} - \text{Var}^{1/2}(\lambda^{ob}|M)$ – as a function of mass. *Right* panel: detection probability as a function of cluster mass. The *dashed* vertical line correspond to the mass at which the detection probability is 50% ($\log M_{50\%} = 14.24[M_{\odot}/h]$). The *blue* area corresponds to the 68% confidence interval derived for the different quantities in this work. For comparison, the results obtained in Murata et al. (2017) are shown in *yellow* in the two left panels.

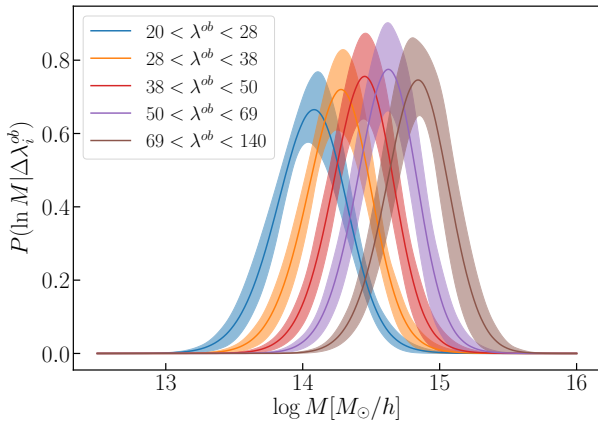


Figure 10. Distribution of halo mass for clusters in each of the five richness bins employed in this work, as labeled. The width of the bands correspond to the 68% confidence interval of the distribution as sampled from our posterior.

mass estimates of 95% of redMaPPer central galaxies correspond to a halo mass of $2 \times 10^{13} h^{-1} M_{\odot}$ or higher. While the stellar-mass to halo-mass relation of central galaxies is relatively uncertain, this result disfavors the existence of a significant population of low-mass ($M \leq 10^{13} h^{-1} M_{\odot}$) redMaPPer clusters, in agreement with our results.

We suspect that the tail of low-mass halos recovered in the Murata et al. (2017) model is responsible for the $\sim 1\sigma$ shift in S_8 seen in Figure 8 when adopting a power-law lognormal model for the richness–mass relation (i.e. the Murata-like analysis): the artificial boost in the abundance of low richness clusters is compensated by a decrease in the predicted halo abundance, which is in turn achieved by lowering the cluster normalization condition.

Finally, the right panel of Figure 9 shows the mass-selection function of the galaxy clusters selected in our experiment. That is, it shows the probability $P(M, z)$ that a halo of mass M at redshift z is included in the SDSS redMaPPer sample. This probability is

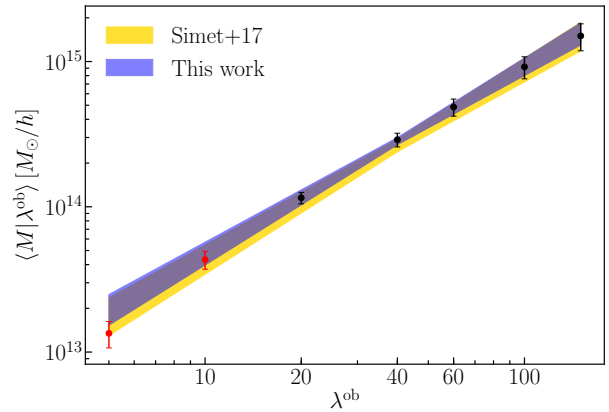


Figure 11. Mass–richness relation derived from the redMaPPer SDSS sample combining cluster abundance and weak lensing data (*blue* area). The data points show the mean mass at a given richness, $\langle M | \lambda^{ob} \rangle$, derived from the posterior distributions of our reference model (see text for details). In analogy with the analysis of Simet et al. (2017) only the *black* points ($\lambda^{ob} > 20$) are used to fit the mass–richness relation. For comparison the mass–richness relation derived in Simet et al. (2017) is shown in *yellow*.

given by

$$P(M, z) = \int_{20}^{\infty} d\lambda^{ob} P(\lambda^{ob} | M, z). \quad (17)$$

The probability $P(M, z)$ is evaluated at a grid of masses for each point in the chain, and the corresponding mean and uncertainty is calculated. Using linear interpolation over this grid, we find that the mass value for which the detection probability is 1/2 is $\log M = 14.24[M_{\odot}/h]$.

Using our best-fit cosmological model we can combine the halo mass function with our recovered richness–mass relation to arrive at our best-fit mass–richness relation. In particular, for each point in the chain we can readily compute $\langle M | \lambda^{ob} \rangle$ along a grid of richnesses, and calculate mean and variance of these quantities at each λ^{ob} value as we sample our posterior. We estimated the mean mass at a grid of values, and computed the corresponding covari-

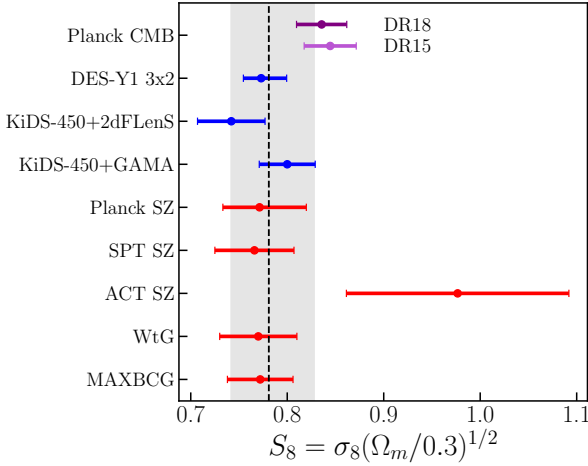


Figure 12. Comparison of the 68% confidence level constraint on S_8 derived from our baseline model (shaded gray area) with other constraints from the literature: red error bars for cluster abundance analyses, blue error bars for weak lensing and galaxy clustering analyses and purple for the CMB constraint. From the bottom to the top: MAXBCG from Rozo et al. (2010); WtG from Mantz et al. (2015); ACT SZ from Hasselfield et al. (2013) (BBN+H0+ACTcl(dyn) in the paper); SPT SZ from de Haan et al. (2016); Planck SZ from Planck Collaboration et al. (2016b) (CCCP+ H_0 +BBN in the paper); KiDs-450+GAMA from van Uitert et al. (2018); KiDs-450+2dFLenS from Joudaki et al. (2018); DES-Y1 3x2 from DES Collaboration et al. (2017a); *Planck* CMB from Planck Collaboration et al. (2016a) (DR15) and Planck Collaboration et al. (2018) (DR18). Note that all the constraints but those from DES-Y1 3x2 and *Planck* CMB have been derived fixing the total neutrino mass either to zero or to 0.06 eV.

ance matrix, and then fit the data with a power-law to arrive at the corresponding mass–richness relation. The resulting mass–richness relation is shown in Figure 11 along with the relation derived in Simet et al. (2017). The posteriors for the mass–richness relation in our analysis is

$$\langle M|\lambda \rangle = 10^{14.45 \pm 0.03} \left(\frac{\lambda}{40} \right)^{1.29 \pm 0.09}, \quad (18)$$

where we used only $\lambda^{\text{ob}} > 20$ data points (black dots in the figure) to fit the power-law relation. This is to be compared to the Simet et al. (2017) relation, $\langle M|\lambda \rangle = 10^{14.42 \pm 0.04} (\lambda/40)^{1.3 \pm 0.1}$. Note that the exponent 14.42 has been obtained correcting the best-fit value 14.37 derived in Simet et al. (2017) assuming $\Omega_m = 0.30$ via Equation 1 using the mean Ω_m value derived in this analysis. Moreover, we expect a small difference in amplitude due to the updates to our multiplicative shear bias model and the redMaPPer centering fraction. All together, these corrections should boost the amplitude of the mass–richness relation by $\approx 6\%$, in good agreement with our results.

7 COMPARISON TO EXTERNAL DATA SETS

Our analysis allows us to place the constraint $S_8 = 0.79^{+0.05}_{-0.04}$. A comparison of our baseline result (gray shaded area) to several other constraints from the literature can be seen in Figure 12. To estimate the level of tension between two analyses A and B we consider the quantity: $T_{A,B} = |\Delta S_8|/\sigma_{\text{tot}}$, where $\sigma_{\text{tot}}^2 = (\sigma_{S_8,A})^2 + (\sigma_{S_8,B})^2$. According to our consistency criterion (see item (v) in Section 5) all the measurements of S_8 from the external data sets

we considered are consistent with the one derived in this analysis ($\Delta S_8 < 3\sigma_{\text{tot}}$). The most significant difference comes with respect to the cluster constraints from the Atacama Cosmology Telescope cluster sample (Hasselfield et al. 2013), though the significance of this difference is still below $2\sigma_{\text{tot}}$. As for the *Planck* DR18 CMB S_8 constraint, the significance of the difference between the two results is only $1.1\sigma_{\text{tot}}$ ¹⁰.

We planned to combine the SDSS redMaPPer cluster abundances constraints with two distinct external data sets, provided that these data sets were consistent with our results (see item (vii) in section 5). Namely we considered:

(i) Baryon Acoustic Oscillation (BAO) data from multiple galaxy surveys, specifically the Six Degree Field Galaxy Survey (6dF Beutler et al. 2011), the SDSS DR 7 Main galaxy sample (Ross et al. 2015), and data from the Baryon Oscillation Spectroscopic Survey (BOSS Alam et al. 2017).

(ii) CMB data from *Planck* satellite, including low l polarization data, from the 2015 data release (hereafter *Planck* DR15; *Planck* Collaboration et al. 2016a).

When combining with BAO data we replace the Gaussian prior on h by a flat prior, while when combining with CMB data we relax all the informative priors on cosmological parameters (i.e. h , $\Omega_b h^2$ and $\Omega_c h^2$, see Table 3) and add the optical depth τ as a free parameter.

According to the protocol detailed in section 5, both data sets passed the consistency criterion required to perform the combined analysis with the SDSS data. Specifically, for the combination of the BAO and SDSS data sets we checked for consistency between Ω_m posteriors, finding the point $p_{\text{SDSS}} - p_{\text{BAO}} = 0$ to lie within the 96.5% confidence level of the $p_{\text{SDSS}} - p_{\text{BAO}}$ distribution. As for the consistency between *Planck* DR15 CMB and SDSS data sets we considered the parameters sub-space (Ω_m, σ_8) , for which we found the point $p_{\text{SDSS}} - p_{\text{CMB}} = 0$ to fall within the 85% confidence level distribution of $p_{\text{SDSS}} - p_{\text{CMB}}$ ¹¹.

Figure 13 shows the 2D marginalized contours for each of the above experiments in the $S_8 - \Omega_m - h$ parameter sub-space (left panels), as well as the posterior for a joint clusters+BAO, and clusters+BAO+*Planck* analysis (right panels). The corresponding 1D marginalized posterior are listed in Table 4.

The combination of galaxy clusters data and BAO measurements results in a precise measurement of the Hubble parameter, $h = 0.66 \pm 0.02$. This value is in excellent agreement and competitive with those derived from *Planck* DR15 CMB data alone $h = 0.66^{+0.02}_{-0.03}$. By contrast, the posterior of h is in 2.7σ tension with the one derived by the SH0ES collaboration using type-Ia supernovae data, $h = 0.732 \pm 0.017$ (Riess et al. 2016), and in 2.1σ tension with the recent strong-lensing based measurement $h = 0.725^{+0.021}_{-0.023}$ presented in Birrer et al. (2018).

The further inclusion of *Planck* DR15 data significantly improve the constraints on all the cosmological parameters considered. Specifically, the errors on Ω_m , σ_8 and h are reduced compared to the SDSS+BAO analysis by a factor of 4, 3 and 2, respec-

¹⁰ The significance of the difference between our S_8 posterior and that of the *Planck* 2015 analysis is $1.2\sigma_{\text{tot}}$.

¹¹ At the time of performing this analysis the latest *Planck* DR18 likelihood is not publicly available. However, the latest *Planck* results (Planck Collaboration et al. 2018) are consistent with the previous data release (Planck Collaboration et al. 2016a) (see Figure 13 for a comparison). According to our consistency criterion, SDSS is consistent also with *Planck* DR18; specifically we find the $p_{\text{SDSS}} - p_{\text{Planck18}} = 0$ point to lie within the 82% confidence distribution of $p_{\text{SDSS}} - p_{\text{Planck18}}$.

Table 4. Parameter constraints from the combination of our analysis of the SDSS redMaPPer cluster abundances with BAO and Planck CMB data sets (see text for details). For reference here are also reported the constraints derived from Planck DR15 CMB and low l polarization data (Planck Collaboration et al. 2016a), BAO data (Beutler et al. 2011; Ross et al. 2015; Alam et al. 2017), and SDSS data alone.

Data sets	Ω_m	σ_8	h	S_8	$\log M_{min}$	$\log M_1$	α	σ_{intr}
Planck15	$0.328^{+0.039}_{-0.026}$	$0.81^{+0.03}_{-0.05}$	$0.662^{+0.019}_{-0.028}$	0.841 ± 0.026	–	–	–	–
BAO	0.373 ± 0.053	–	0.694 ± 0.033	–	–	–	–	–
SDSS	$0.22^{+0.05}_{-0.04}$	$0.91^{+0.11}_{-0.10}$	–	$0.79^{+0.05}_{-0.04}$	11.2 ± 0.2	$12.42^{+0.16}_{-0.13}$	$0.65^{+0.05}_{-0.07}$	< 0.4
SDSS+BAO	0.316 ± 0.036	0.78 ± 0.06	$0.662^{+0.019}_{-0.022}$	$0.792^{+0.039}_{-0.037}$	11.38 ± 0.17	12.63 ± 0.09	0.76 ± 0.05	< 0.2
SDSS+BAO+Planck15	$0.316^{+0.010}_{-0.008}$	0.81 ± 0.02	$0.671^{+0.006}_{-0.008}$	$0.829^{+0.022}_{-0.020}$	11.42 ± 0.15	12.65 ± 0.02	0.76 ± 0.03	< 0.2

tively. Nevertheless, the low-redshift Universe contributes a significant amount of new information: the errors on Ω_m , σ_8 and h for the joint analysis are reduced relative to the *Planck* DR15-only constraints by a factor of 3.6, 2, and 3, respectively.

It is also interesting to investigate the impact that the *Planck* cosmological information has on the parameters governing the richness–mass relation of the redMaPPer clusters. The error on α is reduced from $\sigma_\alpha = 0.06$ to $\sigma_\alpha = 0.03$, while the error on $\log M_1$ goes from $\sigma_{\log M_1} = 0.09$ to $\sigma_{\log M_1} = 0.02$. The factor of four improvement in the $\log M_1$ posterior after adding *Planck* data suggests that the error budget for mass calibration in cluster abundance studies needs to be reduced from the present $\approx 8\%$ to $\approx 2\%$ for *Planck* to add no information to the cluster abundance constraint on S_8 . This value can be compared to the 5% mass calibration achieved by the DES collaboration in McClintock et al. (2018a).

Remarkably, neither the BAO nor the *Planck* data sets improve the posterior on the intrinsic scatter. This may seem surprising given our earlier discussion on the degeneracy between S_8 and σ_{intr} : if tightening the scatter prior improves the S_8 posterior, why does tightening S_8 not improve the scatter posterior? The resolution is evident from Figure 7: the *Planck* data tightens S_8 around the value $S_8 = 0.83$. This S_8 value cuts across the mild S_8 – σ_{intr} degeneracy in such a way that the full range of σ_{intr} values is sampled. Had the *Planck* data favored either a higher or lower S_8 , the posterior on σ_{intr} would have been reduced.

Finally, we find the addition of cluster data has only a modest impact on the posterior on $\sum m_\nu$, from the combination of *Planck* and BAO data. To explore whether future cluster abundance analyses are likely to result in significant improvements we ran chains adopting unrealistically tight 1% priors on the amplitude and slope of the richness–mass relation, as well as a $\sigma_{intr} \leq 0.3$ prior on the scatter. Even in this over-optimistic scenario, clusters had only a minor impact on the posterior for $\sum m_\nu$. This is not entirely unexpected given the small redshift range probed by our cluster catalogue and the fact that the abundance function is only directly sensitive to: 1) $\Omega_{cdm} + \Omega_b$, and 2) the amplitude of the dark matter and baryons power spectrum (e.g. Costanzi et al. 2013). While some sensitivity to $\sum m_\nu$ at a given redshift remains via the volume term in the abundance prediction, the sensitivity to neutrino mass at fixed $\Omega_{cdm} + \Omega_b$ and primordial power spectrum amplitude, A_s , is relatively mild.

8 SUMMARY AND CONCLUSION

We have performed a joint analysis of the abundance and weak lensing mass measurements of the redMaPPer clusters identified in the SDSS DR 8 (Aihara et al. 2011) to simultaneously constrain cosmology and the richness–mass relation parameters. The cosmo-

logical sample consists of 6964 clusters having richness $\lambda^{ob} \geq 20$ in the redshift range $0.1 < z < 0.3$. For the weak lensing mass estimates we employed the results of the stacked weak lensing mass analysis performed by Simet et al. (2017), which achieved a 7.7% precision including both statistical and systematic uncertainties (see Table 2). Our analysis is the first cluster abundance study to be performed while blinded to the recovered cosmological parameters. All the modeling choices and validation tests were made before unblinding the cosmological results. We also verified that our cosmological posteriors are robust to assumptions made about the form and parametrization of the richness–mass relation and systematics associated with the calibration of projection effects (see Figure 8).

Assuming a flat Λ CDM model with massive neutrinos, and including modest H_0 and BBN priors (Cooke et al. 2016), we found $S_8 = 0.79^{+0.05}_{-0.04}$. Our result is in agreement with those obtained by other cluster abundance studies, as well as with constraints derived from the DES Y1 3×2 analysis (DES Collaboration et al. 2017a) and *Planck* DR18 CMB data (Planck Collaboration et al. 2018). The error budget on S_8 is not dominated by a single set of observables; while mass calibration uncertainties are typically the dominant source of error in cluster abundance studies, the uncertainty in the scatter of the richness–mass relation degrades the constraining power of our sample. Since the detailed shape of the abundance function is sensitive to the scatter, the error budget of the abundance data impacts our S_8 posterior at a level comparable to that from our mass-calibration uncertainty. Future analyses that accurately measure the scatter in the richness–mass relation — e.g. from multi-wavelength observations of redMaPPer clusters — will have a significant impact on the cosmological conclusions that can be drawn from optical cluster samples.¹²

Having ascertained the statistical consistency of our data set with *Planck* DR15 CMB data and BAO priors, we combined the SDSS cluster abundance analysis with these two external data sets. From the joint analysis of SDSS and BAO data we obtain $\Omega_m = 0.32 \pm 0.04$, $\sigma_8 = 0.78 \pm 0.06$ and $h = 0.66 \pm 0.02$. These constraints are consistent with and of comparable size to the CMB constraints from *Planck* data. The further inclusion of the *Planck* DR15 data improves the precision of the parameters S_8 , h and α by a factor of 2 and $\log M_1$ by a factor of 4.5. Adding clusters data to *Planck*+BAO has a negligible impact on the posterior of the sum of the neutrino masses, $\sum m_\nu$. This conclusion holds for local cluster surveys even if cluster mass calibration uncertainties decrease to the per-cent level. Table 4 summarizes the posteriors of the SDSS

¹² Given an observational mass proxy X that is known a priori to have substantially lower scatter at fixed mass than richness (e.g. gas mass, or SZ decrement), one can use the joint distribution $P(\lambda, X)$ of the detected clusters to infer the scatter in richness at fixed mass.

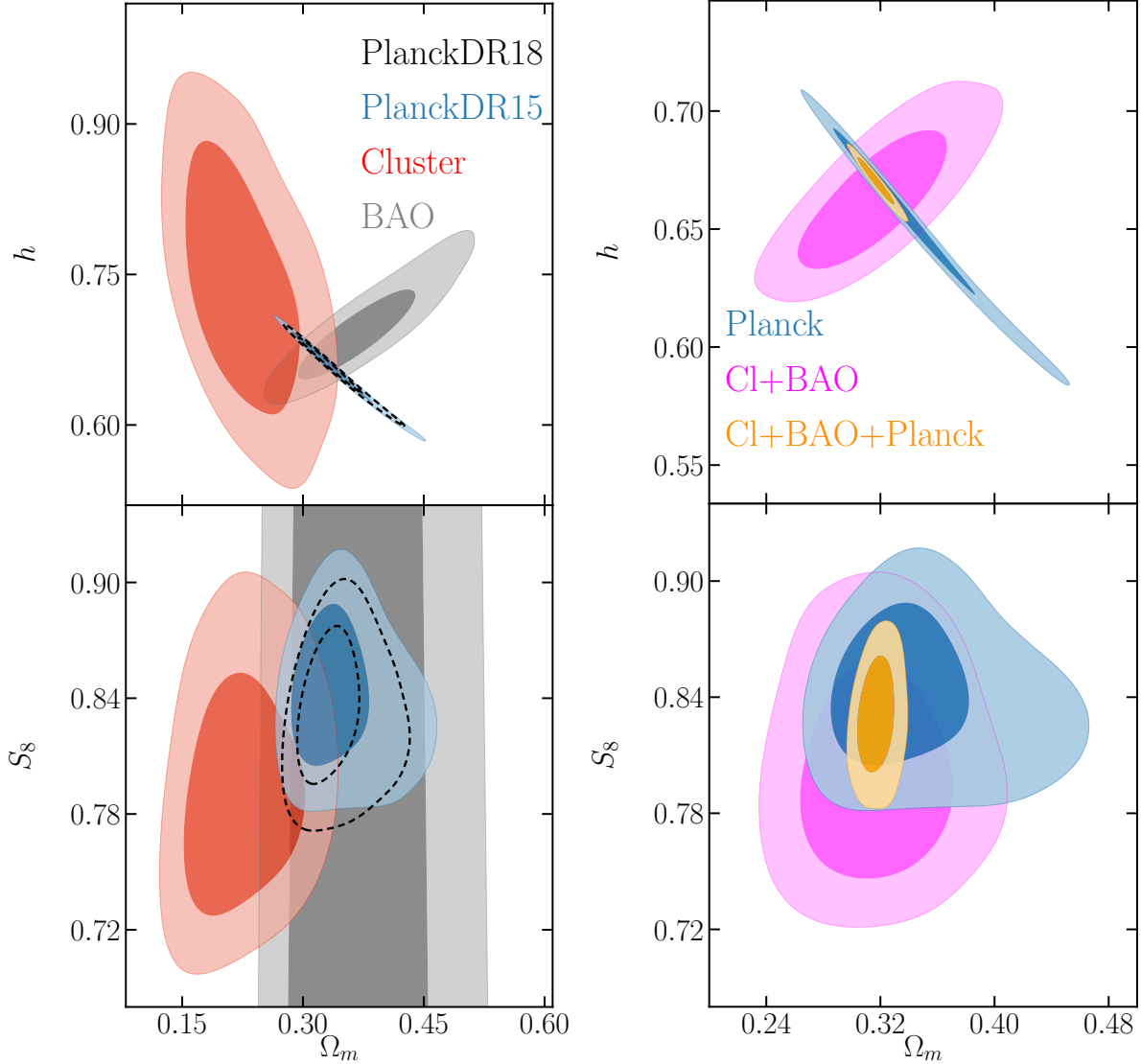


Figure 13. 68% and 95% confidence level constraints in the (S_8, Ω_m, h) plane. *Left panel:* Comparison of the constraints derived from the different data sets considered in this work: *Planck* DR15 (*blue*), BAO (*gray*) and SDSS clusters (*red*). The BAO contours are obtained including the flat prior $\Omega_b h^2 \in [0.0006, 0.01]$, as in the SDSS cluster analysis. Also shown for comparison the latest *Planck* results ((Planck Collaboration et al. 2018); *dashed black lines*). *Right panel:* 68% and 95% confidence contours obtained from the combination of the SDSS cluster sample with BAO data (*magenta*) and from the combination of SDSS clusters, BAO and *Planck* data (*orange*). For comparison, the *blue* contours show the constraints derived from *Planck* CMB data alone. Note the different scales between the *left* and *right* panel.

clusters after combining with the BAO and *Planck* DR15 external data sets.

We have also compared our posteriors on the richness–mass relation to other analyses. In particular, we find that our posterior for the richness–mass relation is in excellent agreement with the results of Murata et al. (2017), except for the lowest richness bin. That work claims $\approx 10\%$ of the clusters in our lowest richness bin have masses $M \leq 10^{13} h^{-1} M_\odot$, whereas we find all our clusters have mass $M \gtrsim 2 \times 10^{13} h^{-1} M_\odot$. We argue that this difference is driven by a theoretical systematic associated with the model adopted in Murata et al. (2017), rather than systematic uncertainties inherent to the data. The stellar mass of the central galaxies in our clusters is consistent with this interpretation. The otherwise excellent agreement between our work and that of Murata et al. (2017) is notable

given the significant methodological differences between the two works.

In short, our results are best summarized by saying that the SDSS cluster abundance data is consistent with the best fit flat Λ CDM cosmology from *Planck*. Our results are also consistent with but have somewhat larger errors than current state-of-the-art analysis combining the auto- and cross-correlations of galaxies and shear (e.g. DES Collaboration et al. 2017a; Joudaki et al. 2018; van Uitert et al. 2018, ; see Figure 12). Future analyses that reduce the mass-calibration uncertainties, combined with measurements of the scatter of the richness–mass relations, will make cluster abundances studies competitive with these combined-clustering results. The first demonstration of this coming power will be the upcoming

analysis of the DES Y1 data set (DES collaboration, in preparation).

ACKNOWLEDGEMENTS

We thank R. Mandelbaum for help and comments with early aspects of this work. This paper has gone through internal review by the DES collaboration. We acknowledge support from the U.S. Department of Energy under contract number DE-AC02-76SF00515. ER was supported by the DOE grant DE-SC0015975, by the Sloan Foundation, grant FG-2016-6443, and the Cottrell Scholar program of the Research Corporation for Science Advancement. Support for DG was provided by NASA through Einstein Postdoctoral Fellowship grant number PF5-160138 awarded by the Chandra X-ray Center, which is operated by the Smithsonian Astrophysical Observatory for NASA under contract NAS8-03060. We thank the AEMULUS collaboration for access to their simulation data products in advance of publication. This research used simulations that were performed resources of the National Energy Research Scientific Computing Center (NERSC), a U.S. Department of Energy Office of Science User Facility operated under Contract No. DE-AC02-05CH11231.

Funding for the DES Projects has been provided by the U.S. Department of Energy, the U.S. National Science Foundation, the Ministry of Science and Education of Spain, the Science and Technology Facilities Council of the United Kingdom, the Higher Education Funding Council for England, the National Center for Supercomputing Applications at the University of Illinois at Urbana-Champaign, the Kavli Institute of Cosmological Physics at the University of Chicago, the Center for Cosmology and Astro-Particle Physics at the Ohio State University, the Mitchell Institute for Fundamental Physics and Astronomy at Texas A&M University, Financiadora de Estudos e Projetos, Fundação Carlos Chagas Filho de Amparo à Pesquisa do Estado do Rio de Janeiro, Conselho Nacional de Desenvolvimento Científico e Tecnológico and the Ministério da Ciência, Tecnologia e Inovação, the Deutsche Forschungsgemeinschaft and the Collaborating Institutions in the Dark Energy Survey.

The Collaborating Institutions are Argonne National Laboratory, the University of California at Santa Cruz, the University of Cambridge, Centro de Investigaciones Energéticas, Medioambientales y Tecnológicas-Madrid, the University of Chicago, University College London, the DES-Brazil Consortium, the University of Edinburgh, the Eidgenössische Technische Hochschule (ETH) Zürich, Fermi National Accelerator Laboratory, the University of Illinois at Urbana-Champaign, the Institut de Ciències de l'Espai (IEEC/CSIC), the Institut de Física d'Altes Energies, Lawrence Berkeley National Laboratory, the Ludwig-Maximilians Universität München and the associated Excellence Cluster Universe, the University of Michigan, the National Optical Astronomy Observatory, the University of Nottingham, The Ohio State University, the University of Pennsylvania, the University of Portsmouth, SLAC National Accelerator Laboratory, Stanford University, the University of Sussex, Texas A&M University, and the OzDES Membership Consortium.

Based in part on observations at Cerro Tololo Inter-American Observatory, National Optical Astronomy Observatory, which is operated by the Association of Universities for Research in Astronomy (AURA) under a cooperative agreement with the National Science Foundation.

The DES data management system is supported by the Na-

tional Science Foundation under Grant Numbers AST-1138766 and AST-1536171. The DES participants from Spanish institutions are partially supported by MINECO under grants AYA2015-71825, ESP2015-66861, FPA2015-68048, SEV-2016-0588, SEV-2016-0597, and MDM-2015-0509, some of which include ERDF funds from the European Union. IFAE is partially funded by the CERCA program of the Generalitat de Catalunya. Research leading to these results has received funding from the European Research Council under the European Union's Seventh Framework Program (FP7/2007-2013) including ERC grant agreements 240672, 291329, and 306478. We acknowledge support from the Australian Research Council Centre of Excellence for All-sky Astrophysics (CAASTRO), through project number CE110001020.

This manuscript has been authored by Fermi Research Alliance, LLC under Contract No. DE-AC02-07CH11359 with the U.S. Department of Energy, Office of Science, Office of High Energy Physics. The United States Government retains and the publisher, by accepting the article for publication, acknowledges that the United States Government retains a non-exclusive, paid-up, irrevocable, world-wide license to publish or reproduce the published form of this manuscript, or allow others to do so, for United States Government purposes.

REFERENCES

- Aihara H., et al., 2011, *ApJS*, 193, 29
 Alam S., et al., 2017, *MNRAS*, 470, 2617
 Allen S. W., Evrard A. E., Mantz A. B., 2011, *ARA&A*, 49, 409
 Anderson L., et al., 2014, *MNRAS*, 441, 24
 Behroozi P. S., Wechsler R. H., Wu H.-Y., 2013, *ApJ*, 762, 109
 Behroozi P., Wechsler R., Hearin A., Conroy C., 2018, preprint, (arXiv:1806.07893)
 Berlind A. A., Weinberg D. H., 2002, *ApJ*, 575, 587
 Beutler F., et al., 2011, *MNRAS*, 416, 3017
 Birrer S., et al., 2018, preprint, (arXiv:1809.01274)
 Bocquet S., Saro A., Dolag K., Mohr J. J., 2016, *MNRAS*, 456, 2361
 Borgani S., et al., 2001, *ApJ*, 561, 13
 Boylan-Kolchin M., Springel V., White S. D. M., Jenkins A., 2010, *MNRAS*, 406, 896
 Brandbyge J., Hannestad S., Haugbølle T., Wong Y. Y. Y., 2010, *J. Cosmology Astropart. Phys.*, 9, 014
 Bullock J. S., Wechsler R. H., Somerville R. S., 2002, *MNRAS*, 329, 246
 Burenin R. A., Vikhlinin A. A., 2012, *Astronomy Letters*, 38, 347
 Busch P., White S. D. M., 2017, *MNRAS*, 470, 4767
 Castorina E., Sefusatti E., Sheth R. K., Villaescusa-Navarro F., Viel M., 2014, *J. Cosmology Astropart. Phys.*, 2, 049
 Cataneo M., et al., 2015, *Phys. Rev. D*, 92, 044009
 Charnock T., Battye R. A., Moss A., 2017, *Phys. Rev. D*, 95, 123535
 Cooke R. J., Pettini M., Nollett K. M., Jorgenson R., 2016, *ApJ*, 830, 148
 Costanzi M., Villaescusa-Navarro F., Viel M., Xia J.-Q., Borgani S., Castorina E., Sefusatti E., 2013, *J. Cosmology Astropart. Phys.*, 12, 012
 Costanzi M., et al., 2018, preprint, (arXiv:1807.07072)
 Crocce M., Fosalba P., Castander F. J., Gaztañaga E., 2010, *MNRAS*, 403, 1353
 Cui W., Borgani S., Murante G., 2014, *MNRAS*, 441, 1769
 DES Collaboration et al., 2017b, preprint, (arXiv:1711.00403)
 DES Collaboration et al., 2017a, preprint, (arXiv:1708.01530)
 Dawson K. S., et al., 2013, *AJ*, 145, 10
 DeRose J., et al., 2018, preprint, (arXiv:1804.05865)
 Despali G., Giocoli C., Angulo R. E., Tormen G., Sheth R. K., Baso G., Moscardini L., 2016, *MNRAS*, 456, 2486
 Diemer B., Kravtsov A. V., 2014, *ApJ*, 789, 1
 Diemer B., Kravtsov A. V., 2015, *ApJ*, 799, 108
 Dietrich J. P., et al., 2014, *MNRAS*, 443, 1713
 Eke V. R., Cole S., Frenk C. S., Patrick Henry J., 1998, *MNRAS*, 298, 1145

Evrard A. E., Arnault P., Huterer D., Farahi A., 2014, MNRAS, 441, 3562
 Farahi A., Evrard A. E., Rozo E., Rykoff E. S., Wechsler R. H., 2016, MNRAS, 460, 3900
 Feldmann R., et al., 2006, MNRAS, 372, 565
 Gelman A., Rubin D. B., 1992, Statistical Science, 7, 457
 Hasselfield M., et al., 2013, J. Cosmology Astropart. Phys., 7, 008
 Henry J. P., 2000, ApJ, 534, 565
 Henry J. P., 2004, ApJ, 609, 603
 Henson M. A., Barnes D. J., Kay S. T., McCarthy I. G., Schaye J., 2017, MNRAS, 465, 3361
 Hikage C., Mandelbaum R., Leauthaud A., Rozo E., Rykoff E. S., 2017, preprint, (arXiv:1702.08614)
 Hinshaw G., et al., 2013, ApJS, 208, 19
 Hirata C., Seljak U., 2003, MNRAS, 343, 459
 Hoekstra H., Herbonnet R., Muzzin A., Babul A., Mahdavi A., Viola M., Cacciato M., 2015, MNRAS, 449, 685
 Hoffmann K., Bel J., Gaztañaga E., 2015, MNRAS, 450, 1674
 Hu W., Cohn J. D., 2006, Phys. Rev. D, 73, 067301
 Hu W., Kravtsov A. V., 2003, ApJ, 584, 702
 Jiang F., van den Bosch F. C., 2016, MNRAS, 458, 2848
 Joudaki S., et al., 2018, MNRAS, 474, 4894
 Knebe A., et al., 2013, MNRAS, 435, 1618
 Koester B. P., et al., 2007, ApJ, 660, 239
 Kravtsov A. V., Borgani S., 2012, ARA&A, 50, 353
 Kravtsov A. V., Berlind A. A., Wechsler R. H., Klypin A. A., Gottlöber S., Allgood B., Primack J. R., 2004, ApJ, 609, 35
 Liu J., Bird S., Zorrilla Matilla J. M., Hill J. C., Haiman Z., Madhavacheril M. S., Petri A., Spergel D. N., 2017, preprint, (arXiv:1711.10524)
 Mana A., Giannantonio T., Weller J., Hoyle B., Hütsi G., Sartoris B., 2013, MNRAS, 434, 684
 Mandelbaum R., Hirata C. M., Leauthaud A., Massey R. J., Rhodes J., 2012, MNRAS, 420, 1518
 Mandelbaum R., Slosar A., Baldauf T., Seljak U., Hirata C. M., Nakajima R., Reyes R., Smith R. E., 2013, MNRAS, 432, 1544
 Mandelbaum R., et al., 2017, preprint, (arXiv:1710.00885)
 Mantz A., Allen S. W., Rapetti D., Ebeling H., 2010, MNRAS, 406, 1759
 Mantz A. B., et al., 2015, MNRAS, 446, 2205
 Mao Y.-Y., Williamson M., Wechsler R. H., 2015, ApJ, 810, 21
 McClintock T., et al., 2018b, preprint, (arXiv:1805.00039)
 McClintock T., et al., 2018a, preprint, (arXiv:1804.05866)
 Medezinski E., et al., 2018, PASJ, 70, 30
 Melchior P., et al., 2017, MNRAS, 469, 4899
 Miyatake H., et al., 2018, preprint, (arXiv:1804.05873)
 Murata R., Nishimichi T., Takada M., Miyatake H., Shirasaki M., More S., Takahashi R., Osato K., 2017, preprint, (arXiv:1707.01907)
 Nakajima R., Mandelbaum R., Seljak U., Cohn J. D., Reyes R., Cool R., 2012, MNRAS, 420, 3240
 Navarro J. F., Frenk C. S., White S. D. M., 1997, ApJ, 490, 493.
 Pierpaoli E., Scott D., White M., 2001, MNRAS, 325, 77
 Planck Collaboration et al., 2016a, A&A, 594, A13
 Planck Collaboration et al., 2016b, A&A, 594, A24
 Planck Collaboration et al., 2018, preprint, (arXiv:1807.06209)
 Reddick R. M., Wechsler R. H., Tinker J. L., Behroozi P. S., 2013, ApJ, 771, 30
 Reiprich T. H., Böhringer H., 2002, ApJ, 567, 716
 Reyes R., Mandelbaum R., Gunn J. E., Nakajima R., Seljak U., Hirata C. M., 2012a, MNRAS, 425, 2610
 Reyes R., Mandelbaum R., Gunn J. E., Nakajima R., Seljak U., Hirata C. M., 2012b, MNRAS, 425, 2610
 Riess A. G., et al., 2016, ApJ, 826, 56
 Ross A. J., Samushia L., Howlett C., Percival W. J., Burden A., Manera M., 2015, MNRAS, 449, 835
 Rozo E., et al., 2010, ApJ, 708, 645
 Rozo E., Rykoff E. S., Becker M., Reddick R. M., Wechsler R. H., 2015, MNRAS, 453, 38
 Rykoff E. S., et al., 2012, ApJ, 746, 178
 Rykoff E. S., et al., 2014, ApJ, 785, 104
 Schaller M., et al., 2015, MNRAS, 451, 1247

Sheth R. K., Tormen G., 1999, MNRAS, 308, 119
 Simet M., McClintock T., Mandelbaum R., Rozo E., Rykoff E., Sheldon E., Wechsler R. H., 2017, MNRAS, 466, 3103
 Sohn J., Geller M. J., Rines K. J., Hwang H. S., Utsumi Y., Diaferio A., 2017, preprint, (arXiv:1712.00872)
 Springel V., 2005, MNRAS, 364, 1105
 Springel V., et al., 2017, arXiv, astro-ph.GA
 Suzuki N., et al., 2012, ApJ, 746, 85
 Takada M., Spergel D. N., 2014, MNRAS, 441, 2456
 Tinker J., Kravtsov A. V., Klypin A., Abazajian K., Warren M., Yepes G., Gottlöber S., Holz D. E., 2008, ApJ, 688, 709
 Tinker J. L., Robertson B. E., Kravtsov A. V., Klypin A., Warren M. S., Yepes G., Gottlöber S., 2010, ApJ, 724, 878
 Velliscig M., van Daalen M. P., Schaye J., McCarthy I. G., Cacciato M., Le Brun A. M. C., Dalla Vecchia C., 2014, MNRAS, 442, 2641
 Vikhlinin A., et al., 2009, ApJ, 692, 1033
 Villaescusa-Navarro F., Marulli F., Viel M., Branchini E., Castorina E., Sefusatti E., Saito S., 2014, J. Cosmology Astropart. Phys., 3, 011
 Wechsler R. H., Tinker J. L., 2018, preprint, (arXiv:1804.03097)
 Zehavi I., et al., 2011, ApJ, 736, 59
 Zheng Z., et al., 2005, ApJ, 633, 791
 Zu Y., Mandelbaum R., Simet M., Rozo E., Rykoff E. S., 2017, MNRAS, 470, 551
 de Haan T., et al., 2016, ApJ, 832, 95
 van Uitert E., et al., 2018, MNRAS, 476, 4662
 von der Linden A., et al., 2014a, MNRAS, 439, 2
 von der Linden A., et al., 2014b, MNRAS, 443, 1973

APPENDIX A: CLUSTER NUMBER COUNTS COVARIANCE MATRIX

The covariance matrix for the cluster number counts is computed adding the different contributions listed in Section 3.3:

$$C = C^{\text{Poisson}} + C^{\text{SampVar}} + C^{\text{Misc}}. \quad (\text{A1})$$

The first two terms, which account for the statistical uncertainty, are computed analytically along the MCMC for the relevant cosmological and model parameters. The Poisson contribution to the covariance matrix is simply given by the expectation value for the number counts in the specific bin (cf. Equation 2):

$$C^{\text{Poisson}} = \delta_{ii} \langle N \rangle_i \quad (\text{A2})$$

The sample variance terms read (Hu & Kravtsov 2003)

$$C_{ij}^{\text{SampVar}} = \langle bN(\Delta\lambda_i^{\text{ob}}, \Delta z_i^{\text{ob}}) \rangle \langle bN(\Delta\lambda_j^{\text{ob}}, \Delta z_j^{\text{ob}}) \rangle \sigma^2(V_i, V_j) \quad (\text{A3})$$

where the first two terms are defined as:

$$\langle bN(\Delta\lambda_i^{\text{ob}}, \Delta z_i^{\text{ob}}) \rangle = \int_0^\infty dz^{\text{true}} \Omega_{\text{mask}} \frac{dV}{dz^{\text{true}} d\Omega} \int_{\Delta z_i^{\text{ob}}} dz^{\text{ob}} P(z^{\text{ob}} | z^{\text{true}})_{\Delta\lambda_i^{\text{ob}}} \int dM b(M, z) n(M, z) \int_{\Delta\lambda_i^{\text{ob}}} d\lambda^{\text{ob}} P(\lambda^{\text{ob}} | M, z) \quad (\text{A4})$$

and the last one corresponds to the rms variance of the linear density field:

$$\sigma^2(V_i, V_j) = \int \frac{d\mathbf{k}}{(2\pi)^3} \sqrt{P_L(k, z_i) P_L(k, z_j)} W_i(\mathbf{k}) W_j(\mathbf{k}). \quad (\text{A5})$$

Here, $b(M, z)$ is the linear halo bias for which we use the Tinker et al. (2010) formula, V_i is the comoving volume corresponding to the redshift bin z_{ob} , and $W_i(\mathbf{k})$ the Fourier transform of the window function. Approximating the survey mask with a top-hat window

symmetric around the azimuthal axis, and setting the angular area $\Omega_{\text{mask}} = 2\pi(1 - \cos(\theta_s))$ equal to the total survey area, $W_i(\mathbf{k})$ reads:

$$W_i(\mathbf{k}) = \left(\frac{dV}{d\Omega} \Big|_{\Delta z_i} \right)^{-1} \int_{\Delta z_i} dz \frac{dV}{dz d\Omega} 4\pi \sum_{l=0}^{\infty} \sum_{m=-l}^l (i)^l j_l(k\chi(z)) Y_{l,m}(\hat{\mathbf{k}}) K_l \quad (\text{A6})$$

where $j_l(x)$ are the spherical Bessel functions, $\chi(z)$ is the comoving distance to redshift z , $Y_{l,m}(\hat{\mathbf{k}})$ are the spherical harmonics, and K_l the coefficients of the expansion in spherical harmonics of the angular part of the window function:

$$\text{for } l = 0 \quad K_l = \frac{1}{2\sqrt{\pi}} \quad (\text{A7})$$

$$\text{for } l \neq 0 \quad K_l = \sqrt{\frac{\pi}{2l+1}} \frac{P_{l-1}(\cos(\theta_s)) - P_{l+1}(\cos(\theta_s))}{\Omega_{\text{mask}}},$$

where $P_l(x)$ are the Legendre polynomials.

Finally, the term due to the miscentering correction, C^{Misc} , is estimated numerically from 1000 realizations of the number counts data (corrected for the miscentering error) obtained sampling the offset distribution parameters from their priors as described in Zhang et al., in preparation.

APPENDIX B: SKEW-NORMAL APPROXIMATION

The richness–mass relation $P(\lambda^{\text{true}}|M)$ is a convolution of a Poissonian and a Gaussian distribution. In this work, we approximate the resulting convolution with a skew-normal distribution:

$$P(\lambda^{\text{true}}|M) = \frac{1}{\sqrt{2\pi\sigma^2}} e^{-\frac{(\lambda^{\text{true}} - \langle \lambda^{\text{sat}}|M \rangle)^2}{2\sigma^2}} \text{erfc} \left[-\alpha \frac{\lambda^{\text{true}} - \langle \lambda^{\text{sat}}|M \rangle}{\sqrt{2\sigma^2}} \right]. \quad (\text{B1})$$

The values of the model parameters α and σ vary as a function of the expectation value $\langle \lambda^{\text{sat}}|M \rangle$ and intrinsic scatter σ_{intr} . We derive these values by fitting the skew-normal distribution to realizations of a normal-Poissonian convolution obtained by varying $\langle \lambda^{\text{sat}}|M \rangle$ and σ_{intr} along the relevant range of values for this analysis. Each $P(\lambda^{\text{true}})$ realization is generated from 10^6 realizations of the true richness obtained as $\lambda^{\text{true}} = 1 + \Delta^{\text{Poisson}} + \Delta^{\text{Gauss}}$, where Δ^{Poisson} is a random number drawn from a Poisson distribution having mean $\langle \lambda^{\text{sat}} \rangle$ and Δ^{Gauss} a random number drawn from a Gaussian distribution having null mean and scatter equal to $\sigma_{\text{intr}} \langle \lambda^{\text{sat}} \rangle$. Figure B1 compares the histograms obtained from these realizations to the resulting best fit skew-normal distribution. We calibrate the parameters of the skew-normal distribution along a dense grid in $\langle \lambda^{\text{sat}} \rangle$ and σ_{intr} and linearly interpolate along this 2D grid to define the skew-normal parameters at every point in parameter space.

AFFILIATIONS

¹ Universitäts-Sternwarte, Fakultät für Physik, Ludwig-Maximilians Universität München, Scheinerstr. 1, 81679 München, Germany

² Department of Physics, University of Arizona, Tucson, AZ 85721, USA

³ Department of Physics and Astronomy, University of California Riverside, 900 University Ave, Riverside, CA 92521, USA

⁴ Fermi National Accelerator Laboratory, P. O. Box 500, Batavia, IL 60510, USA

⁵ Department of Astronomy, University of Michigan, Ann Arbor, MI 48109, USA

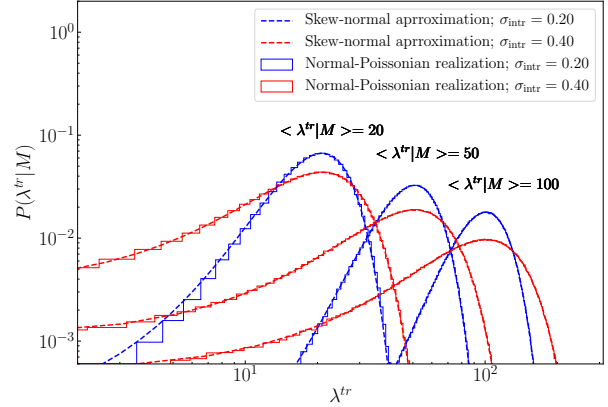


Figure B1. Comparison of the convolution of a normal and Poissonian distribution (*histograms*) with a skew-normal distribution (*solid lines*) for different values of $\langle \lambda^{\text{sat}}|M \rangle$ and σ_{intr} (see labels).

⁶ Department of Physics, University of Michigan, Ann Arbor, MI 48109, USA

⁷ Kavli Institute for Particle Astrophysics & Cosmology, P. O. Box 2450, Stanford University, Stanford, CA 94305, USA

⁸ SLAC National Accelerator Laboratory, Menlo Park, CA 94025, USA

⁹ Santa Cruz Institute for Particle Physics, Santa Cruz, CA 95064, USA

¹⁰ Department of Physics, Stanford University, 382 Via Pueblo Mall, Stanford, CA 94305, USA

¹¹ Department of Physics and Astronomy, Pevensey Building, University of Sussex, Brighton, BN1 9QH, UK

¹² Department of Physics and Astronomy, Stony Brook University, Stony Brook, NY 11794, USA

¹³ Department of Physics, Carnegie Mellon University, Pittsburgh, Pennsylvania 15312, USA

¹⁴ Max Planck Institute for Extraterrestrial Physics, Giessenbachstrasse, 85748 Garching, Germany

¹⁵ Excellence Cluster Universe, Boltzmannstr. 2, 85748 Garching, Germany

¹⁶ Department of Physics and Astronomy, Pevensey Building, University of Sussex, Brighton, BN1 9QH, UK

¹⁷ Cerro Tololo Inter-American Observatory, National Optical Astronomy Observatory, Casilla 603, La Serena, Chile

¹⁸ Department of Physics & Astronomy, University College London, Gower Street, London, WC1E 6BT, UK

¹⁹ Department of Physics and Electronics, Rhodes University, PO Box 94, Grahamstown, 6140, South Africa

²⁰ Institute of Cosmology & Gravitation, University of Portsmouth, Portsmouth, PO1 3FX, UK

²¹ LSST, 933 North Cherry Avenue, Tucson, AZ 85721, USA

²² Laboratório Interinstitucional de e-Astronomia - LIneA, Rua Gal. José Cristino 77, Rio de Janeiro, RJ - 20921-400, Brazil

²³ Observatório Nacional, Rua Gal. José Cristino 77, Rio de Janeiro, RJ - 20921-400, Brazil

²⁴ Department of Astronomy, University of Illinois at Urbana-Champaign, 1002 W. Green Street, Urbana, IL 61801, USA

²⁵ National Center for Supercomputing Applications, 1205 West Clark St., Urbana, IL 61801, USA

²⁶ Institut de Física d'Altes Energies (IFAE), The Barcelona Institute of Science and Technology, Campus UAB, 08193 Bellaterra (Barcelona) Spain

- ²⁷ Institut d'Estudis Espacials de Catalunya (IEEC), 08193 Barcelona, Spain
- ²⁸ Institute of Space Sciences (ICE, CSIC), Campus UAB, Carrer de Can Magrans, s/n, 08193 Barcelona, Spain
- ²⁹ Centro de Investigaciones Energéticas, Medioambientales y Tecnológicas (CIEMAT), Madrid, Spain
- ³⁰ Faculty of Physics, Ludwig-Maximilians-Universität, Scheinerstr. 1, 81679 Munich, Germany
- ³¹ Department of Astronomy/Steward Observatory, 933 North Cherry Avenue, Tucson, AZ 85721-0065, USA
- ³² Jet Propulsion Laboratory, California Institute of Technology, 4800 Oak Grove Dr., Pasadena, CA 91109, USA
- ³³ Kavli Institute for Cosmological Physics, University of Chicago, Chicago, IL 60637, USA
- ³⁴ Instituto de Física Teórica UAM/CSIC, Universidad Autónoma de Madrid, 28049 Madrid, Spain
- ³⁵ Institute of Astronomy, University of Cambridge, Madingley Road, Cambridge CB3 0HA, UK
- ³⁶ Kavli Institute for Cosmology, University of Cambridge, Madingley Road, Cambridge CB3 0HA, UK
- ³⁷ Department of Physics, ETH Zurich, Wolfgang-Pauli-Strasse 16, CH-8093 Zurich, Switzerland
- ³⁸ Center for Cosmology and Astro-Particle Physics, The Ohio State University, Columbus, OH 43210, USA
- ³⁹ Department of Physics, The Ohio State University, Columbus, OH 43210, USA
- ⁴⁰ Harvard-Smithsonian Center for Astrophysics, Cambridge, MA 02138, USA
- ⁴¹ Australian Astronomical Observatory, North Ryde, NSW 2113, Australia
- ⁴² Departamento de Física Matemática, Instituto de Física, Universidade de São Paulo, CP 66318, São Paulo, SP, 05314-970, Brazil
- ⁴³ Department of Physics and Astronomy, University of Pennsylvania, Philadelphia, PA 19104, USA
- ⁴⁴ George P. and Cynthia Woods Mitchell Institute for Fundamental Physics and Astronomy, and Department of Physics and Astronomy, Texas A&M University, College Station, TX 77843, USA
- ⁴⁵ Department of Astronomy, The Ohio State University, Columbus, OH 43210, USA
- ⁴⁶ Institució Catalana de Recerca i Estudis Avançats, E-08010 Barcelona, Spain
- ⁴⁷ Brookhaven National Laboratory, Bldg 510, Upton, NY 11973, USA
- ⁴⁸ School of Physics and Astronomy, University of Southampton, Southampton, SO17 1BJ, UK
- ⁴⁹ Brandeis University, Physics Department, 415 South Street, Waltham MA 02453
- ⁵⁰ Instituto de Física Gleb Wataghin, Universidade Estadual de Campinas, 13083-859, Campinas, SP, Brazil
- ⁵¹ Computer Science and Mathematics Division, Oak Ridge National Laboratory, Oak Ridge, TN 37831

This paper has been typeset from a $\text{\TeX}/\text{\LaTeX}$ file prepared by the author.